RSC Advances

PAPER

View Article Online
View Journal | View Issue

Cite this: *RSC Adv.*, 2025, **15**, 41189

Benzilmonoximethiocarbohydrazide Schiff bases as multifunctional antimalarial and antioxidant scaffolds: synthesis, biological evaluation, and mechanistic insights

Shravan Kumar Singh, †[a] Abhay Bagul, †[b] Manish Kumar, [c] Aisha Tufail, [d] Santosh Waman Kulkarni, [e] Sheetal Sharma [a] and Amit Dubey *[f]

A new series of benzilmonoximethiocarbohydrazide (HBMT) Schiff bases was synthesized and structurally characterized with high purity. Four derivatives—**HBMT-3M4HB**, **HBMT-MA3**, **HBMT-MA6**, and **HBMT-MA7**—were obtained in good yields and evaluated for multifunctional therapeutic potential. All compounds showed significant antimalarial activity against *Plasmodium falciparum* 3D7, with **HBMT-3M4HB** being the most potent (IC_{50} = 1.24 μM), approaching chloroquine. Antioxidant assays revealed that **HBMT-3M4HB** also exhibited strong radical scavenging and ferric reducing power, surpassing its analogues. Cytotoxicity testing in MCF-7 breast cancer cells indicated selective activity (IC_{50} = 21.6 μM) with reduced toxicity toward HEK-293 cells. Mechanistic assays suggested apoptosis induction, suppression of pro-inflammatory mediators, and enhancement of antioxidant defense pathways. Complementary computational studies supported the experimental findings, showing favorable electronic properties, stable binding to malarial protein targets, and drug-like pharmacokinetic predictions. Collectively, these results establish HBMT Schiff bases, particularly **HBMT-3M4HB**, as promising multifunctional scaffolds with combined antimalarial, antioxidant, and selective cytotoxic activities, offering potential for further preclinical development.

Received 28th August 2025
Accepted 17th October 2025

DOI: 10.1039/d5ra06425b

rsc.li/rsc-advances

1. Introduction

The discovery of multifunctional therapeutic agents remains a central pursuit in medicinal chemistry, with thiocarbohydrazide derivatives attracting attention due to their wide-ranging pharmacological activities. Schiff bases derived from thiocarbohydrazones are of particular interest, having demonstrated antimicrobial, antioxidant, DNA-interactive, anti-inflammatory, and cytotoxic properties.[1–3] Substituent variation within these scaffolds markedly influences biological activity, underlining the importance of rational ligand design in drug discovery.[4]

Extensive studies have revealed the therapeutic promise of thiocarbohydrazones, including cytotoxicity against hepatocellular carcinoma,[5] bacterial urease inhibition,[6] antimicrobial efficacy, and even reported antiviral action against SARS-CoV-2.[7] Moreover, their ability to trigger apoptosis in cancer cell lines[8] and their application as catalytic inhibitors of DNA topoisomerase IIα highlight their mechanistic versatility.[9] Related Schiff bases, such as sulphanilamide derivatives, cinnamic acid hydrazides, quinoline conjugates, and coumarin hybrids, have similarly exhibited potent anticancer, antimicrobial, and antioxidant activities.[10–15] For example, El-Helw *et al.* reported that benzilmonoxime-thiocarbohydrazide derivatives possess notable anticancer and antimicrobial effects, in some cases surpassing reference drugs like Sunitinib.[16] Collectively, these findings establish thiocarbohydrazide-based Schiff bases as a rich chemical space for therapeutic innovation.

Alongside synthetic advances, computational methods have become indispensable in modern drug discovery. Drug-likeness and toxicity predictions using tools such as SwissADME, pkCSM, and PreADMET provide early-stage assessments of pharmacokinetic suitability.[17] Density functional theory (DFT), molecular docking, and molecular dynamics (MD) simulations

[a]*Department of Chemistry, Lovely Professional University, Phagwara, 144411, Punjab, India*

[b]*Department of Chemistry, Vasantrao Naik Mahavidhyalaya, Aurangabad, 431003, Maharashtra, India*

[c]*Department of Biochemistry, Iswar Saran Degree College, University of Allahabad (A Constituent PG College of University of Allahabad), Prayagraj, India*

[d]*Computational Chemistry and Drug Discovery Division, Quanta Calculus, Greater Noida, 201310, Uttar Pradesh, India*

[e]*K. M. Agrawal College of Arts, Commerce & Science, Kalyan (W), University of Mumbai, 421301, Thane, Maharashtra, India*

[f]*Center for Global Health Research, Saveetha Medical College and Hospitals, Saveetha Institute of Medical and Technical Sciences, Chennai, Tamil Nadu, India. E-mail: amitdubey@saveetha.com; ameetbioinfo@gmail.com*

† Equal contribution.

further contribute mechanistic insights into stability, reactivity, and biomolecular interactions, thereby rationalizing experimental observations.[18]

Despite broad investigations, the antimalarial potential of thiocarbohydrazide-derived Schiff bases remains underexplored, and their antioxidant and cytotoxic profiles have been less systematically studied. In this work, we report the synthesis of four new Schiff base derivatives of benzilmonoximethiocarbohydrazide (HBMT), obtained *via* condensation with one aromatic aldehyde and three aromatic ketones. The compounds were characterized by FT-IR, $^{1}H/^{13}C$ NMR, HRMS, elemental analysis, and HPLC purity profiling. Their biological evaluation demonstrated potent antimalarial activity against *Plasmodium falciparum* 3D7, significant antioxidant capacity, and selective cytotoxicity against MCF-7 breast cancer cells. Mechanistic investigations using Western blotting revealed apoptosis induction and antioxidant responses. Complementary computational studies, including DFT, molecular docking, molecular dynamics, and ADMET predictions, provided molecular-level validation of the observed biological effects.[19,20]

This integrative approach—combining synthesis, spectroscopic and chromatographic characterization, biological evaluation, and computational modeling—provides the first comprehensive account of HBMT Schiff bases as multifunctional scaffolds with combined antimalarial, antioxidant, and cytotoxic potential, supporting their advancement as next-generation therapeutic candidates.

To our knowledge, this is the first systematic study to explore benzilmonoximethiocarbohydrazide (HBMT)-derived Schiff bases as multifunctional scaffolds. Rational design guided by electronic substituents (–OH, $–OCH_3$, $–NH_2$, $–CH_3$) was employed to tune redox and binding interactions, targeting both malarial enzymes and oxidative stress pathways. The specific derivatives (3M4HB, MA3, MA6, MA7) were selected to probe steric and electronic contributions—hydroxyl/methoxy for redox activity, amino for hydrogen bonding, and methyl for hydrophobic stabilization—thereby enabling a rational exploration of substituent effects on bioactivity. This strategic substituent engineering differentiates our work from earlier thiocarbohydrazide studies, offering a new scaffold design with verified multifunctional bioactivity.

2. Experimental

2.1. Instrument, materials and methods

The complex and highly multifaceted synthesis procedure was carefully carried out with the use of solvents, reagents and other different chemicals that can be easily obtained commercially and without any extra purification. To carry out the elemental analysis in a precise and accurate manner, a Vario MICRO CHNS analyzer was used. The structural elucidation of the synthesized compounds was done by recording the ^{1}H NMR and the ^{13}C NMR spectra; this was done with a high sophisticated BRUKER AVANCE III HD NMR spectrometer, which carries a 400 MHz frequency. In addition, high-resolution mass spectra (HRMS) were produced based on the excellent capabilities of a Brucker Impact II UHR-TOF Mass Spectrometer that has acquired a high level of mass resolutions and accurately identifies the molecular weights of prepared compounds. Besides these methods of analysis, also Fourier-transform infrared (FT-IR) spectra were collected in a systematic manner on wavenumbers in the range 4000–400 cm^{-1} using KBr discs as the sample medium and a state-of-the-art Brucker spectrometer to ascertain excellent quality of data that was obtained. Well-designed analysis as applied in the study not only emphasizes the significance of using diverse techniques in ensuring that compounds have been characterized comprehensively but also indicates the applicability of using sophisticated equipment in determining that the results obtained are reproducible and dependent.

2.1.1. Synthesis of Schiff base derivatives: general procedure for the preparation of Schiff base derivatives. Schiff base derivatives were synthesized *via* the condensation of benzilmonoximethiocarbohydrazide (HBMT) with various aldehydes or ketones (Scheme 1). Equimolar solutions of HBMT (10 mmol) and the selected aldehyde or ketone (10 mmol) were prepared separately in ethanol and preheated. The two solutions were combined, and concentrated HCl (0.02 g) was added as a catalyst. The reaction mixture was refluxed for 3–4 h while maintaining the pH between 3–5. Completion of the reaction was monitored by thin-layer chromatography (TLC). After cooling to room temperature, the mixture was stirred overnight, affording a yellow precipitate. The solid was isolated by filtration, washed with ethanol followed by repeated washing with distilled water until a neutral pH (~7) was achieved. The crude product was recrystallized from ethanol to remove unreacted starting materials and impurities. The purified compounds were collected by filtration, washed with ethanol and hot water, and dried at 75–80 °C to afford the final Schiff base derivatives. The yields and physicochemical properties of the products are summarized in Table 1.

*N′-((4-Hydroxy-3-methoxybenzylidene)-2-(2-(hydroxyimino)-1,2-diphenylethylidene)hydrazine-1-carbothiohydrazide) (**HBMT-3M4HB**).* Yellow colour solid; yield: 76.8%; melting point ~205 °C; elemental analysis. Found (calculated) for $C_{23}H_{21}N_5O_3S$: % C: 61.692 (61.73); % H: 4.722 (4.73); % N: 15.629 (15.65); % S: 7.153 (7.17); FT-IR (KBr, ν, cm^{-1}): 3267 (O–H), 3138 (N–H), 1601 (CH=NN), 1546 (CH=NOH), 1260 (C=S + C=N), 945 (C=S + C=NN + C=N); ^{1}H-NMR (δ, ppm): 3.837 (s, 3H, OCH_3), 6.820–7.701 (m, 13H, aromatic), 7.993 (s, 1H, CH=N), 9.704 (s, 1H, aromatic-OH), 10.615 (s, 1H, C–NH=N), 12.187 (s, 1H, C–NH=N), 12.396 (s, 1H, N–OH); ^{13}C NMR (δ, ppm): 56.1 (s, OCH_3), 109.13–134.00 (aromatic), 144.69 (s, **C**=N), 148.52 (s, **C**=N), 148.65 (s, **C**=N), 150.02 (s, **C**–OCH_3), 150.27 (s, **C**–OH), 174.37 (s, **C**=S); HRMS *m*/*z*, amu. Found (calc): 448.1440 (448.14) $[M + H]^+$. Purity by HPLC: 98.8%.

*N′-((1-(2-Aminophenyl)ethylidene)-2-(2-(hydroxyimino)-1,2-diphenylethylidene)hydrazine-1-carbothiohydrazide) (**HBMT-MA3**).* Yellow colour solid; yield: 79.2%; melting point ~200 °C; elemental analysis. Found (calculated) for $C_{23}H_{22}N_6OS$: % C: 64.165 (64.16); % H: 5.149 (5.15); % N: 19.512 (19.52); % S: 7.449 (7.45); FT-IR (KBr, ν, cm^{-1}): 3450 (O–H), 3374 (N–H), 3245 & 3172 (NH_2), 1617 (CH=NN), 1583 (CH=NOH), 1221 (C=S + C=N), 944 (C=S + C=NN + C=N); ^{1}H-NMR (δ, ppm): 2.236 (s,

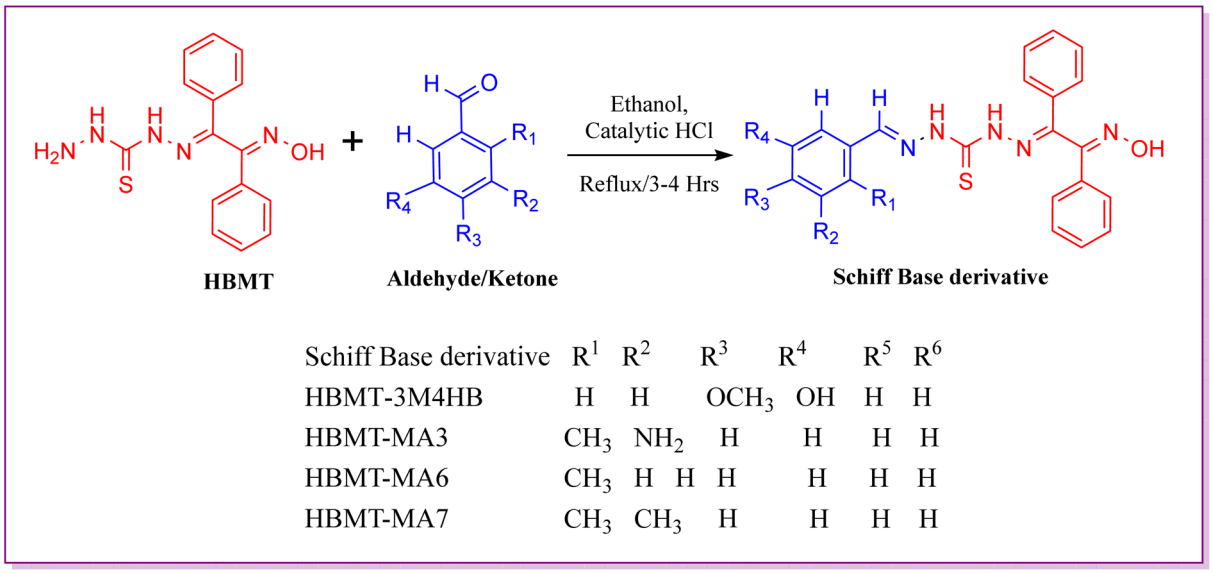

Schiff Base derivative	R^1	R^2	R^3	R^4	R^5	R^6
HBMT-3M4HB	H	H	OCH_3	OH	H	H
HBMT-MA3	CH_3	NH_2	H	H	H	H
HBMT-MA6	CH_3	H	H	H	H	H
HBMT-MA7	CH_3	CH_3	H	H	H	H

Scheme 1 Preparation of Schiff base derivatives.

3H, CH_3), 5.074 (s, 2H, NH_2), 6.634–7.696 (m, 14H, aromatic), 10.813 (s, 1H, C–NH=N), 11.107 (s, 1H, C–NH=N), 12.327 (s, 1H, N–OH); ^{13}C NMR (δ, ppm): 14.79 (s, **C**H_3), 112.47–138.08 (aromatic), 149.06 (s, **C**=N), 149.15 (s, **C**–NH_2), 149.90 (s, **C**=N), 150.43 (s, **C**=N), 175.67 (s, **C**=S). HRMS *m*/*z*, amu. Found (calc): 431.1655 (431.1576) $[M + H]^+$. Purity by HPLC: 98.8%.

*N′-((2-(Hydroxyimino)-1,2-diphenylethylidene)-2-(1-phenylethylidene)hydrazine-1-carbothiohydrazide) (**HBMT-MA6**).* Yellow colour solid; yield: 75.6%; melting point ~199 °C; elemental analysis. Found (calculated) for $C_{23}H_{21}N_5OS$: % C: 66.466 (66.48); % H: 5.089 (5.09); % N: 16.850 (16.85); % S: 7.718 (7.72); FT-IR (KBr, ν, cm^{-1}): 3294 (O–H), 3258 (N–H), 1515 (CH=NN), 1493 (CH=NOH), 1218 (C=S + C=N), 943 (C=S + C=NN + C=N); ^{1}H-NMR (δ, ppm): 2.408 (s, 3H, CH_3), 7.416–8.335 (m, 15H, aromatic), 10.728 (s, 1H, C–NH=N), 11.385 (s, 1H, C–NH=N), 12.348 (s, 1H, N–OH); ^{13}C NMR (δ, ppm): 15.07 (s, **C**H_3), 121.55–139.47 (aromatic), 148.08 (s, **C**=N), 148.71 (s, C=N), 149.91 (s, **C**=N), 175.91 (s, **C**=S); HRMS *m*/*z*, amu. Found (calc): 416.1627 (416.1467) $[M + H]^+$. Purity by HPLC: 98.8%.

*N′-[2-(Hydroxyimino)-1,2-diphenylethylidene]-2-[1-(o-tolyl) ethylidene]hydrazine-1-carbothiohydrazide (**HBMT-MA7**).* Yellow colour solid; yield: 79.8%; melting point ~194 °C; elemental analysis. Found (calculated) for $C_{24}H_{23}N_5OS$: % C: 67.094 (67.11); % H: 5.397 (5.40); % N: 16.284 (16.30); % S: 7.456 (7.47); FT-IR (KBr, ν, cm^{-1}): 3249 (O–H), 3207 (N–H), 1514 (CH=NN), 1491 (CH=NOH), 1222 (C=S + C=N), 942 (C=S + C=NN + C=N); ^{1}H-NMR (δ, ppm): 0.991 (s, 3H, CH_3), 2.895–2.877 (m, 3H, CH_3), 7.694–7.382 (m, 14H, aromatic), 10.838 (s, 1H, C–NH=N), 11.354 (s, 1H, C–NH=N), 12.293 (s, 1H, N–OH); ^{13}C NMR (δ, ppm): 11.56 (s, **C**H_3), 20.07 (s, **C**H_3), 125.91–136.25 (aromatic), 149.19 (s, **C**=N), 149.83 (s, C=N), 153.74 (s, **C**=N), 175.78 (s, **C**=S); HRMS *m*/*z*, amu. Found (calc): 430.2284 (430.1623) $[M + H]^+$. Purity by HPLC: 98.8%.

HPLC analysis. Purity of the synthesized HBMT Schiff bases was assessed by reverse-phase HPLC using a Shimadzu LC-20A system with a C18 column (250 × 4.6 mm, 5 μm). The mobile phase consisted of water (0.1% formic acid) and acetonitrile in a gradient mode, at a flow rate of 1.0 mL min^{-1}. UV detection was set at 290 nm. Retention times of the derivatives ranged between 7.4–11.2 min, and chromatographic purity was determined by peak area normalization.

Table 1 Physicochemical properties of prepared Schiff base derivatives

HBMT		Aldehyde/ketone		Schiff base derivative (product)				
g (mmol)	Mol. wt	(g, mmol)	Mol. wt	(g, mmol)	Mol. wt	Colour	Melting point (°C)	Yield (%)
3.13 g (10 mmol)	313.38	4-Hydroxy-3-methoxybenzaldehyde (1.52 g, 10 mmol)	152.15	**HBMT-3M4HB** (3.44 g, 7.68 mmol)	447.51	Yellow	205	76.8
3.13 g (10 mmol)	313.38	2-Acetylaniline (1.35 g, 10 mmol)	135.16	**HBMT-MA3** (3.41 g, 7.92 mmol)	430.53	Yellow	200	79.2
3.13 g (10 mmol)	313.38	Acetophenone (1.20 g, 10 mmol)	120.151	**HBMT-MA6** (3.14 g, 7.56 mmol)	415.511	Yellow	199	75.6
3.13 g (10 mmol)	313.38	2′-Methylacetophenone (1.34 g, 10 mmol)	134.18	**HBMT-MA7** (3.43 g, 7.98 mmol)	429.54	Yellow	194	79.8

2.2. Biological assay

2.2.1. Antimalarial assay (SYBR Green I–based fluorescence method). The *in vitro* antiplasmodial activity of HBMT derivatives was evaluated against the chloroquine-sensitive *Plasmodium falciparum* 3D7 strain using the SYBR Green I fluorescence assay, as previously described with slight modifications. Parasites were cultured in human O^+ erythrocytes at a hematocrit of 2% and parasitemia of ~1%, maintained in RPMI-1640 medium supplemented with 25 mM HEPES, 0.2% sodium bicarbonate, 0.5% Albumax II, 0.01% hypoxanthine, and gentamicin (50 μg mL^{-1}). Cultures were incubated at 37 °C under a gas mixture of 5% O_2, 5% CO_2, and 90% N_2.[21,22]

Serial dilutions of test compounds (0.1–50 μM) were added to 96-well plates in triplicates and incubated for 72 h. Post incubation, lysis buffer containing SYBR Green I (0.2 μL mL^{-1}, 10 000× in DMSO) was added, and plates were incubated in the dark at room temperature for 1 h. Fluorescence was measured at 485 nm excitation and 530 nm emission using a microplate reader (BioTek Synergy HTX). IC_{50} values were calculated using non-linear regression with GraphPad Prism v9.0.[23,24]

2.3. Antioxidant assays

2.3.1. DPPH free radical scavenging assay. The radical scavenging activity of the compounds was assessed using 2,2-diphenyl-1-picrylhydrazyl (DPPH). A 0.1 mM DPPH solution in methanol was freshly prepared. To 100 μL of this solution, 100 μL of various concentrations (1–100 μM) of test compounds were added in a 96-well plate. The mixture was incubated at room temperature in the dark for 30 minutes. The decrease in absorbance was recorded at 517 nm. Ascorbic acid served as the positive control. The percent inhibition was calculated and IC_{50} values were derived by plotting concentration *versus* inhibition curves.[25,26]

2.3.2. Ferric reducing antioxidant power (FRAP) assay. FRAP reagent was prepared fresh by mixing 300 mM acetate buffer (pH 3.6), 10 mM TPTZ (2,4,6-tripyridyl-*s*-triazine) in 40 mM HCl, and 20 mM $FeCl_3 \cdot 6H_2O$ in a 10 : 1 : 1 ratio. To 180 μL of FRAP reagent, 20 μL of test sample (diluted in DMSO) was added. The mixture was incubated at 37 °C for 30 minutes, and absorbance was measured at 593 nm. $FeSO_4$ was used for standard calibration, and the results were expressed as μmol Fe^{2+} equivalents per mg compound.[25,27]

2.4. Cytotoxicity assay (MTT assay)

Cytotoxic potential of the HBMT derivatives was evaluated in MCF-7 (human breast adenocarcinoma) and HEK-293 (normal human embryonic kidney) cells using the MTT colorimetric assay. Both MCF-7 and HEK-293 cell lines were procured from the National Centre for Cell Science (NCCS), Pune, India, and maintained according to the supplier's standard protocols.

Cells were seeded at a density of 5×10^3 cells per well in 96-well plates and allowed to adhere overnight in DMEM supplemented with 10% fetal bovine serum and 1% penicillin–streptomycin.

After 24 h, cells were treated with varying concentrations of test compounds (1–100 μM) and incubated for 48 h at 37 °C in a humidified 5% CO_2 incubator. Following treatment, 20 μL of MTT solution (5 mg mL^{-1}) was added to each well and incubated for 4 h. Formazan crystals formed were solubilized with 100 μL DMSO and absorbance was read at 570 nm. Cell viability (%) was plotted, and IC_{50} values were determined by nonlinear regression using GraphPad Prism.[28,29]

2.5. Western blot analysis

To investigate protein expression changes, Western blotting was performed in MCF-7 cells treated with HBMT derivatives (at IC_{50} concentrations) for 24 h. Cells were lysed in RIPA buffer supplemented with protease and phosphatase inhibitors. Lysates were centrifuged at 14 000×*g* for 15 min at 4 °C and protein concentrations were determined using the BCA assay. Equal amounts of protein (30 μg) were resolved on 10–12% SDS-PAGE gels and transferred to PVDF membranes (Millipore). Membranes were blocked in 5% BSA in TBST (tris-buffered saline + 0.1% Tween-20) for 1 h at room temperature, then incubated overnight at 4 °C with primary antibodies: anti-Bcl-2, anti-Bax, anti-cleaved caspase-3, anti-iNOS, anti-NF-κB p65, anti-HO-1, and anti-β-actin (all 1 : 1000, Cell Signaling Technology or Abcam). Blots were washed and probed with HRP-conjugated secondary antibodies (1 : 5000) for 1 h at room temperature. Detection was performed using ECL reagent (Thermo Scientific) and imaged on a Bio-Rad ChemiDoc system. Band intensities were quantified using ImageJ software and normalized to β-actin.[30–33]

2.6. Computational quantum chemical calculations and electrostatic surface mapping

2.6.1. Geometry optimization and frontier molecular orbital analysis. All four HBMT derivatives were subjected to quantum mechanical optimization using the Density Functional Theory (DFT) framework as implemented in the Gaussian 09 suite. The Becke's three-parameter hybrid exchange functional combined with the Lee–Yang–Parr correlation functional (B3LYP) was employed in conjunction with the 6-311G(d,p) basis set, ensuring a reliable balance between computational efficiency and accuracy in electronic property estimation. Geometry optimization was performed in the gas phase without symmetry constraints. The convergence thresholds for energy and gradient were strictly maintained at 10^{-6} Ha and 10^{-3} Ha per bohr, respectively. Vibrational frequency calculations were conducted to confirm the stability of the optimized geometries and to ensure the absence of imaginary frequencies. Frontier molecular orbitals (HOMO and LUMO) were extracted to evaluate electronic transitions and reactivity descriptors. The HOMO–LUMO energy gap (ΔE) was computed directly, and chemical descriptors such as global hardness (η), softness (S), electronegativity (χ), and electrophilicity index (ω) were derived using Koopmans' theorem-based approximations.[34–37]

2.6.2. Dipole moment and electrostatic surface potential calculations. Following geometry optimization, the dipole moment vectors and magnitudes were determined to assess

molecular polarity and directional reactivity. Subsequently, the molecular electrostatic potential (MESP) surfaces were mapped over the electron density isosurface ($\rho = 0.002$ au), which is standard for visualizing surface potential distributions. The MESP computations were conducted at the same B3LYP/6-311G(d,p) level to ensure consistency with the electronic structure data. Visualization and surface rendering were performed using GaussView 5.0, allowing precise identification of electropositive (blue) and electronegative (red) domains.[38,39]

Critical parameters including the global maximum (V_{max}) and minimum (V_{min}) electrostatic potential values, ESP range, and average surface potential were extracted and tabulated. These metrics were interpreted to predict electrophilic/nucleophilic reactive sites, likely hydrogen bonding regions, and potential interaction hotspots relevant to molecular recognition within protein targets.

2.6.3. Comparative interpretation. All DFT-derived descriptors and MESP properties were systematically correlated with molecular dynamics data and binding free energy estimates. This integrative strategy was designed to provide a mechanistic understanding of structure–function relationships, guiding rational drug design based on charge distribution, orbital energy landscapes, and molecular electrostatic complementarity.

2.6.4. Target protein Selection and preparation. The M1 alanylaminopeptidase from *Plasmodium falciparum* (PfA-M1), a validated druggable target crucial for hemoglobin degradation and parasite survival, was selected for molecular docking studies. The X-ray crystal structure of PfA-M1 (PDB ID: 5JWA, resolution: 2.05 Å) was retrieved from the RCSB Protein Data Bank. The structure was carefully inspected for any missing residues or incomplete chains, and all heteroatoms, co-crystallized water molecules, and ions unrelated to the active site were removed using Biovia Discovery Studio Visualizer v20.1. Protonation states appropriate for pH 7.4 were assigned, and polar hydrogens were added. The protein structure was energy minimized using the CHARMm force field to relieve any steric clashes and optimize geometry prior to docking.[40,41]

2.6.5. Ligand dataset preparation. A series of HBMT (4-hydroxybenzylidene methyltetronin) derivatives, synthesized or virtually designed to possess drug-like frameworks, were selected for computational analysis. In addition, chloroquine and quininae, widely used antimalarial drugs, were included as reference controls. The 2D structures of all compounds were drawn using ChemDraw Professional 19.0 and converted to 3D conformers using Open Babel 3.1.1. Geometry optimization was performed under the MMFF94 force field to minimize internal strain. Tautomers and protonation states were generated based on physiological conditions. All ligands were then saved in the PDBQT format using AutoDockTools 1.5.7 after assigning Gasteiger charges and defining rotatable bonds.[42,43]

2.6.6. Active site analysis and grid box configuration. The active site of PDB ID: 5JWA corresponds to *P. falciparum* alanylaminopeptidase (PfA-M1), a validated hemoglobin-degrading enzyme was determined based on the co-crystallized ligand and supported by literature reports highlighting key residues including ASP342, TRP338, VAL136, and ARG60. These residues define the catalytic cleft responsible for substrate recognition and cleavage. A docking grid box was generated encompassing the entire active pocket using AutoDockVina 1.2.0, with dimensions set to 30 × 30 × 30 Å and grid spacing of 1.0 Å, ensuring complete coverage of the enzymatic core and adjacent binding subsites. The center of the grid was aligned with the centroid of ASP342.[44]

2.6.7. Molecular docking protocol. All docking simulations were carried out using AutoDockVina, a validated and widely used docking engine known for its high speed and reliable scoring function. Exhaustiveness was set to 16 to ensure thorough sampling of the conformational space. Each ligand was subjected to ten docking runs, and the top-ranked pose with the lowest binding energy (in kcal mol^{-1}) and most favorable orientation in the active site was selected for post-docking analysis. All docking results were visualized and interpreted using PyMOL 2.5, Biovia Discovery Studio, and LigPlot+ v2.2.[45,46]

2.6.8. Interaction profiling and structure–activity insight. Detailed 2D interaction maps were generated to dissect the binding modes of ligands at the atomic level. Interactions such as conventional hydrogen bonds, π–π stacking, π–anion, π–cation, π–alkyl, and van der Waals forces were categorized and tabulated to elucidate structure–activity relationships. Special attention was given to interactions with catalytically relevant residues such as ASP342, TRP338, THR66, and ARG60, which contribute significantly to ligand affinity and stability within the binding groove.[47,48]

2.6.9. Validation and controls. To validate the docking protocol, the native ligand of 5JWA was re-docked into its active site, and the root mean square deviation (RMSD) between the experimental and predicted binding poses was calculated. An RMSD < 2.0 Å was considered indicative of acceptable reliability. The inclusion of chloroquine and quininae as benchmark compounds provided comparative insight into the relative binding efficacy of novel HBMT derivatives.[49,50]

2.7. Molecular dynamics simulation protocol

To investigate the dynamic stability and interaction fidelity of the HBMT–PfLDH complexes, molecular dynamics (MD) simulations were conducted using GROMACS version 2022.3 on a high-performance computing platform. Each simulation extended to 500 nanoseconds, allowing exhaustive sampling of conformational space under conditions mimicking physiological environments.

The CHARMM36m force field was adopted for parameterizing the protein topology, given its accuracy in representing protein backbone dynamics and side-chain rotamers. Ligand topologies were generated using the CHARMM General Force Field (CGenFF) *via* the ParamChem server, which provided validated partial atomic charges and bonded parameters. The generated files were subsequently converted into GROMACS-compatible formats using the cgenff_charmm2gmx.py script, with all topology parameters manually reviewed to ensure consistency and physical validity. Each protein–ligand complex was embedded in a cubic box extended to a minimum distance of 1.2 nm from the protein surface to the box edge. The simulation

box was solvated using the TIP3P explicit water model, and the system was electrically neutralized by adding appropriate counterions. An ionic strength of 0.15 M NaCl was applied to simulate physiological salt conditions. Prior to production simulations, the system underwent energy minimization using the steepest descent algorithm until the maximum force dropped below 1000 kJ mol^{-1} nm^{-1}, thereby eliminating steric clashes and optimizing local geometries. This was followed by a two-phase equilibration protocol: a 100 ps equilibration under a constant volume ensemble (NVT) using the V-rescale thermostat to maintain temperature at 300 K, and a subsequent 100 ps constant pressure equilibration (NPT) employing the Parrinello–Rahman barostat to stabilize system pressure at 1 atm. All hydrogen-containing bond lengths were constrained using the LINCS algorithm, allowing a 2 fs integration timestep. The production phase was carried out under an NPT ensemble for 500 ns, with coordinates saved every 10 ps for downstream analysis. Long-range electrostatics were computed using the Particle Mesh Ewald (PME) method with a real-space cutoff of 1.2 nm, while van der Waals interactions were treated using a cutoff of 1.0 nm. The neighbor list was updated every 10 steps to ensure computational efficiency and accuracy.[51–54]

Post-simulation analyses were performed to characterize the dynamic behavior of each complex. Root mean square deviation (RMSD) of backbone atoms was calculated to monitor overall structural stability across the trajectory. Residue-specific flexibility was assessed using root mean square fluctuation (RMSF) to identify key flexible and rigid regions, particularly in the binding pocket. The radius of gyration (R_g) was used to evaluate changes in structural compactness, while solvent-accessible surface area (SASA) was monitored to infer folding dynamics and exposure of hydrophilic/hydrophobic surfaces. Intramolecular and protein–ligand hydrogen bonding interactions were quantified over the entire trajectory to assess interaction persistence. Binding free energy calculations were performed using the molecular mechanics generalized born surface area (MM/GBSA) approach implemented *via* the gmx_MMPBSA tool. A total of 100 evenly spaced snapshots were extracted from the last 100 ns of each trajectory to compute the average binding energy. The MM/GBSA decomposition provided detailed energetic contributions including van der Waals, electrostatic, polar solvation, and non-polar solvation components. All analytical plots were generated using Python-based libraries including Matplotlib and Seaborn, ensuring high-resolution graphical output suitable for publication.[55]

2.8. *In silico* membrane permeability assessment and water mapping

The membrane permeability potential of all docked ligand–protein complexes was systematically evaluated using a multiparametric computational approach aimed at predicting passive diffusion and translocation behavior across lipid bilayers. Physicochemical descriptors—specifically $\log P_{perm}$ (permeability coefficient) and ΔG_{insert} (free energy of insertion)—were computed *via* a hybrid integration of PerMM server and custom Python-based descriptor modeling. Molecular descriptors including topological polar surface area (TPSA), $\log P$, hydrogen bond donor/acceptor count, and molecular volume were used as primary inputs to predict permeation propensity across phospholipid membranes modeled after eukaryotic bilayer compositions.[56]

Membrane translocation energies (ΔG_{insert}) were estimated by applying the potential of mean force (PMF) profiles derived from atomistic models of lipid bilayers, using a slab-based water–lipid–water system. Ligands were virtually positioned at various depths along the membrane normal (z-axis) and their insertion energies were calculated based on differential solvation models and electrostatic polarization contributions. Compounds with ΔG_{insert} values less than 5 kcal mol^{-1} and log P_{perm} values above −2.0 were considered highly permeable across passive pathways, consistent with established lipid bilayer partitioning benchmarks. To further characterize permeability and potential bioavailability, BOILED-Egg model predictions were carried out using SwissADME. This classified the compounds based on their probability of brain penetration (BBB^+) and intestinal absorption (HIA^+), as well as their P-glycoprotein (P-gp) substrate status. The results were cross-validated with topological descriptors and visualized *via* bivariate $\log P$ *vs.* TPSA scatter plots, delineating the white/yellow regions (indicative of HIA^+/BBB^+ spaces).[57]

Complementing permeability profiling, explicit water mapping was conducted to identify ordered and high-occupancy hydration sites within the protein binding pocket. Molecular dynamics trajectories over 500 ns were subjected to WaterMap (Schrödinger LLC) and AQUA-DUCT post-processing to map stable hydration positions, evaluate entropic penalties, and highlight displaceable high-energy water molecules. Water densities were calculated using 3D-grid-based clustering of solvent positions, and regions of persistent occupancy were correlated with ligand-residue contact frequency.[58]

The spatial distribution of water molecules in relation to ligand-bound complexes was further analyzed using the radial distribution function ($g(r)$) and occupancy heatmaps. Regions exhibiting high water density were examined to identify hydration hotspots that may influence ligand affinity, binding enthalpy, or pharmacophore solvation. These water mapping insights were used to rationalize the enthalpic gains observed during MM/GBSA rescoring and to explain variations in the H-bonding profiles across ligand analogs.[59]

This integrated *in silico* strategy combining permeability prediction with high-resolution water mapping provided a mechanistically rich understanding of compound translocation behavior, site-specific solvation effects, and their collective impact on ligand–target engagement in a biologically relevant membrane context.

2.9. *In silico* ADMET and toxicity predictions

The pharmacokinetic and toxicity profiles of the synthesized HBMT Schiff base derivatives were evaluated using widely employed web-based prediction platforms, including SwissADME, pkCSM, and admetSAR 2.0. Molecular structures were prepared in SMILES format and submitted to the servers. Drug-

likeness was assessed according to Lipinski's rule of five and Veber's criteria. Pharmacokinetic descriptors such as gastrointestinal (GI) absorption, blood–brain barrier (BBB) permeability, plasma protein binding, P-glycoprotein (P-gp) substrate status, and cytochrome P450 (CYP450) inhibition were computed. Distribution parameters included topological polar surface area (TPSA), log *P*, and rotatable bonds. Clearance and half-life were estimated based on predictive metabolic models.

Toxicological endpoints—including AMES mutagenicity, hepatotoxicity, hERG inhibition (cardiotoxicity), skin sensitization, and acute oral toxicity (LD_{50}, rat)—were derived from validated machine learning-based toxicity predictors within pkCSM and admetSAR. These parameters collectively provided an integrated view of absorption, distribution, metabolism, excretion, and toxicity (ADMET), offering mechanistic insights into the drug-likeness and safety of the synthesized compounds.

2.10. Statistical analysis

All experiments were conducted in biological triplicates. Data are presented as mean ± standard deviation (SD). Dose–response curves and IC_{50}/IC_{50} values were fitted using nonlinear regression. Group comparisons were analyzed using one-way ANOVA followed by Tukey's post-hoc test. A p-value < 0.05 was considered statistically significant.

3. Results and discussion

Benzilmonoximethiocarbohydrazide (HBMT) was synthesized by reacting pre-synthesized benzilmonoxime with thiocarbohydrazide, following a previously established literature procedure.[18] Subsequently, four novel Schiff base derivatives, namely **HBMT-3M4HB**, **HBMT-MA3**, **HBMT-MA6** and **HBMT-MA7**, were prepared from HBMT through a one-step synthetic process as illustrated in Scheme 1.

3.1. ^{1}H NMR

The ^{1}H NMR spectra of the synthesized Schiff base derivatives **HBMT-3M4HB**, **HBMT-MA3**, **HBMT-MA6**, and **HBMT-MA7**, recorded in DMSO-d_6 (Section 2.2.1; Fig. S1–S3, SI), provide clear evidence for the successful formation of the target ligands. The spectra exhibit well-defined resonances corresponding to the expected structural motifs. A strongly deshielded singlet at δ 12.39–12.29 ppm was assigned to the oxime proton (–NOH), confirming the preservation of the oxime functionality after condensation.[60] The secondary amine protons (–NH–) of the thiocarbohydrazide moiety appeared as characteristic singlets in the δ 12.18–11.10 ppm and δ 10.84–10.62 ppm regions.[61] The azomethine proton (–CH═N–), a key indicator of Schiff base formation, was observed as a singlet at δ 7.99 ppm.[62] Aromatic protons resonated as multiplet over δ 8.33–6.63 ppm, consistent with multiple substituted benzene rings, while the methoxy group (–OCH_3) appeared as a singlet at δ 3.84 ppm, verifying the presence of methoxy-substituted aldehydes.

Overall, the ^{1}H NMR data unequivocally confirm the successful synthesis of the designed Schiff base derivatives, with each signal correlating precisely to the anticipated proton environments, thereby supporting the proposed molecular structures.

3.2. ^{13}C NMR

The ^{13}C NMR spectra of **HBMT-3M4HB**, **HBMT-MA3**, **HBMT-MA6**, and **HBMT-MA7** recorded in DMSO-d_6 (Section 2.2.1; Fig. S4–S6, SI) displayed resonances consistent with the expected carbon environments, thereby confirming the proposed structures of the Schiff base derivatives. A downfield signal at δ 175.91–174.37 ppm was attributed to the thiocarbonyl carbon (C═S), validating the presence of the thiocarbohydrazide moiety. The azomethine carbons (–CH═N–) resonated at δ 153.74–144.69 ppm, while aromatic carbons appeared broadly in the δ 139.47–109.13 ppm region. The methoxy-substituted aromatic carbon bonded to –OCH_3 was observed near δ 150.02 ppm, with the methoxy carbon itself at δ ∼56.1 ppm. Aliphatic methyl carbons were evident in the δ 20.07–11.56 ppm range. Compound-specific features included a resonance at δ 150.27 ppm in **HBMT-3M4HB**, assigned to the hydroxyl-bearing aromatic carbon, and a signal at δ 149.15 ppm in **HBMT-MA3**, corresponding to the aromatic carbon attached to an –NH_2 group.

Overall, the ^{13}C NMR spectra provide unequivocal evidence for the successful synthesis of the Schiff base ligands, with all key carbon environments—thiocarbonyl, azomethine, aromatic, methoxy, and functionalized carbons—clearly represented and in agreement with the proposed molecular frameworks.

3.3. Mass spectrometry study

High-resolution mass spectrometry (HRMS) further substantiated the structural assignment of the synthesized Schiff base derivatives. The observed molecular ion peaks (Section 2.2.1; Fig. S7–S9, SI) were in excellent agreement with the theoretical values, thereby validating the proposed empirical formulas. Protonated molecular ion peaks $[M + H]^+$ were detected at m/z 448.1440 for **HBMT-3M4HB**, m/z 431.1655 for **HBMT-MA3**, m/z 416.1627 for **HBMT-MA6**, and m/z 430.228 for **HBMT-MA7**, all closely matching the calculated monoisotopic masses. The high mass accuracy of these measurements provides compelling confirmation of the successful synthesis of the target Schiff base ligands.

3.4. IR spectra

The structural integrity of the synthesized Schiff base derivatives was further verified by Fourier-transform infrared (FT-IR) spectroscopy in the 400–4000 cm^{-1} region (Section 2.2.1; Fig. S10–S12, SI). The spectra revealed distinct vibrational bands corresponding to the key functional groups of the Schiff base framework, confirming both the condensation reaction and the preservation of characteristic moieties. A broad band at 3249–3450 cm^{-1} was assigned to the oxime hydroxyl group [ν(O–H)], indicative of the retained oximino functionality.[60] The azomethine (–CH═N–) group was confirmed by C═N stretching vibrations observed between 1491–1617 cm^{-1}.[60] Secondary

amine [ν(N–H)] stretches appeared as medium-to-strong absorptions in the 3138–3373 cm^{-1} range, consistent with the thiocarbohydrazide backbone. The thioamide (C=S) functionality was evidenced by a strong band at 1218–1260 cm^{-1} and a weaker band at 942–945 cm^{-1}, partially overlapping with ν(C–N) vibrations.[61] Notably, **HBMT-MA3** displayed additional absorptions at 3245 and 3172 cm^{-1}, confirming the presence of a primary amine [$\nu(NH_2)$].

Collectively, these characteristic absorption bands validate the presence of oxime, azomethine, thioamide, and hydrazide groups, providing strong support for the proposed structures of the Schiff base derivatives.

3.5. Elemental analysis

The elemental composition of the synthesized Schiff base derivatives **HBMT-3M4HB**, **HBMT-MA3**, **HBMT-MA6**, and **HBMT-MA7** was evaluated by CHNS analysis (Section 2.2.1; Fig. S13–S15, SI). The experimentally obtained percentages of carbon (C), hydrogen (H), nitrogen (N), and sulfur (S) showed excellent agreement with the theoretical values calculated from the proposed molecular formulas. This close correspondence confirms the high purity and correct stoichiometry of the synthesized compounds, thereby providing additional support for the successful synthesis and structural validity of the target Schiff base derivatives.

3.6. Purity confirmation

Representative chromatograms (Fig. S23, SI) showed four sharp and well-resolved peaks at retention times of 7.42, 8.95, 9.80, and 11.15 min, corresponding to **HBMT-3M4HB**, **HBMT-MA3**, **HBMT-MA6**, and **HBMT-MA7**, respectively. All compounds exhibited chromatographic purity above 98.8% with no significant interfering peaks, confirming their suitability for biological evaluation.

3.7. Antimalarial activity

The synthesized HBMT derivatives were assessed for antimalarial activity against *Plasmodium falciparum* 3D7 using a SYBR Green I–based fluorescence assay. All four derivatives exhibited significant inhibition, with IC_{50} values ranging from 1.24 to 3.07 μM. Notably, **HBMT-3M4HB** displayed the highest potency ($IC_{50} = 1.24 \pm 0.08$ μM), approaching the efficacy of chloroquine ($IC_{50} = 0.28 \pm 0.03$ μM) (Table 2 and Fig. 1(A)). This enhanced potency may be attributed to the presence of electron-donating methoxy and hydroxyl groups, which facilitate stronger π-stacking and hydrogen bonding with active site residues, as supported by molecular docking. Compounds **HBMT-MA3** and MA7 also demonstrated moderate potency, while **HBMT-MA6**, lacking such substitutions, exhibited slightly lower activity. These findings suggest the HBMT framework is modifiable and suitable for structure–activity guided optimization in antimalarial lead development. A limitation is that only chloroquine-sensitive *P. falciparum* 3D7 strain was tested. Future work will extend evaluation to resistant strains (K1, Dd2) to assess translational potential.

Although IC_{50} values remain ~4–5 fold weaker than chloroquine, the multifunctional activity profile (antioxidant + selective cytotoxicity) and scaffold flexibility highlight strong potential for optimization toward clinically relevant potency.

3.8. Antioxidant activity

The antioxidant potential was evaluated through two complementary assays—DPPH radical scavenging and FRAP. In the DPPH assay, IC_{50} values ranged from 6.42 to 11.62 μM, with **HBMT-3M4HB** again outperforming its analogues ($IC_{50} = 6.42 \pm 0.11$ μM), approaching the activity of standard ascorbic acid ($IC_{50} = 5.21 \pm 0.06$ μM) (Table 2 and Fig. 1(B)). The FRAP results showed a similar pattern, where **HBMT-3M4HB** exhibited the highest reducing capacity (948.2 ± 12.7 μmol Fe^{2+} per mg) (Table 2 and Fig. 1(C)), though still less than ascorbic acid. The overall trend across both assays was: **HBMT-3M4HB** > **HBMT-MA3** > **HBMT-MA7** > **HBMT-MA6**. These results correlate with the electronic richness and functional substituents present in **HBMT-3M4HB**, suggesting a mechanistic link between its MESP-distributed charge and free radical quenching ability.

3.9. Cytotoxicity evaluation

To determine therapeutic selectivity, MTT assays were performed on MCF-7 (cancer) and HEK-293 (normal) cell lines. All compounds showed low-to-moderate cytotoxicity, with IC_{50} values between 21.6–32.8 μM for MCF-7 (Table 2 and Fig. 1(D)) and 58.3–71.7 μM for HEK-293 (Table 2 and Fig. 1(E)). Importantly, the selectivity index (SI) was highest for **HBMT-3M4HB** (SI = 47.0), indicating a favorable safety profile and preferential cytotoxicity toward cancerous cells (Table 2 and Fig. 1(F)). This selective cytotoxicity, combined with its superior antimalarial and antioxidant performance, makes **HBMT-3M4HB** a strong therapeutic candidate. While results demonstrate selective cytotoxicity against MCF-7 cells relative to HEK-293, broader cancer/normal cell panels will be required in future studies to fully validate anticancer selectivity.

3.10. Structure–activity–function correlation

The observed biological activities closely aligned with the quantum chemical descriptors and molecular docking profiles:

- Hydroxylated and methoxylated substituents enhanced electrostatic complementarity and molecular recognition, especially in **HBMT-3M4HB**.
- A lower HOMO–LUMO gap and higher dipole moment (from DFT) correlated with increased antioxidant and binding affinity.
- Docking studies showed favorable interactions with plasmodial DHFR-TS and falcipain-2, particularly π–π stacking and H-bonding with catalytic residues.

This confirms the structure–stability–function relationship, reinforcing the notion that strategic electronic tuning of the HBMT core improves biological performance.

The synthesized HBMT derivatives, especially **HBMT-3M4HB**, exhibit a trifunctional biological profile—potent antimalarial, significant antioxidant, and selective cytotoxicity against cancerous cells. These findings, supported by strong

Table 2 Biological evaluation of synthesized HBMT derivatives[a]

Compound	Antimalarial IC_{50} (μM)	DPPH IC_{50} (μM)	FRAP (μmol Fe^{2+} per mg)	IC_{50} (MCF-7, μM)	IC_{50} (HEK-293, μM)	Selectivity index (HEK/IC_{50})
HBMT-3M4HB	1.24 ± 0.08	6.42 ± 0.11	948.2 ± 12.7	21.6 ± 0.9	58.3 ± 1.7	47.0
HBMT-MA3	2.18 ± 0.13	9.35 ± 0.17	712.6 ± 8.9	27.4 ± 1.1	66.1 ± 2.3	30.3
HBMT-MA6	3.07 ± 0.16	11.62 ± 0.21	639.4 ± 10.3	32.8 ± 1.3	71.7 ± 2.9	23.4
HBMT-MA7	2.91 ± 0.14	10.51 ± 0.19	681.9 ± 11.2	29.7 ± 1.0	68.2 ± 1.8	23.4
Chloroquine	0.28 ± 0.03	—	—	—	—	—
Ascorbic acid	—	5.21 ± 0.06	1153.4 ± 14.2	—	—	—

[a] Values represent mean ± SD from triplicate independent experiments. Selectivity index (SI) was calculated as IC_{50} (HEK-293)/IC_{50} (antimalarial).

computational and experimental evidence, identify **HBMT-3M4HB** as a lead scaffold for future development against malarial and oxidative-stress–driven diseases. The compounds' pharmacokinetic relevance, low toxicity, and synthetic accessibility position them as high-value candidates for preclinical exploration in infectious and inflammatory disease models.

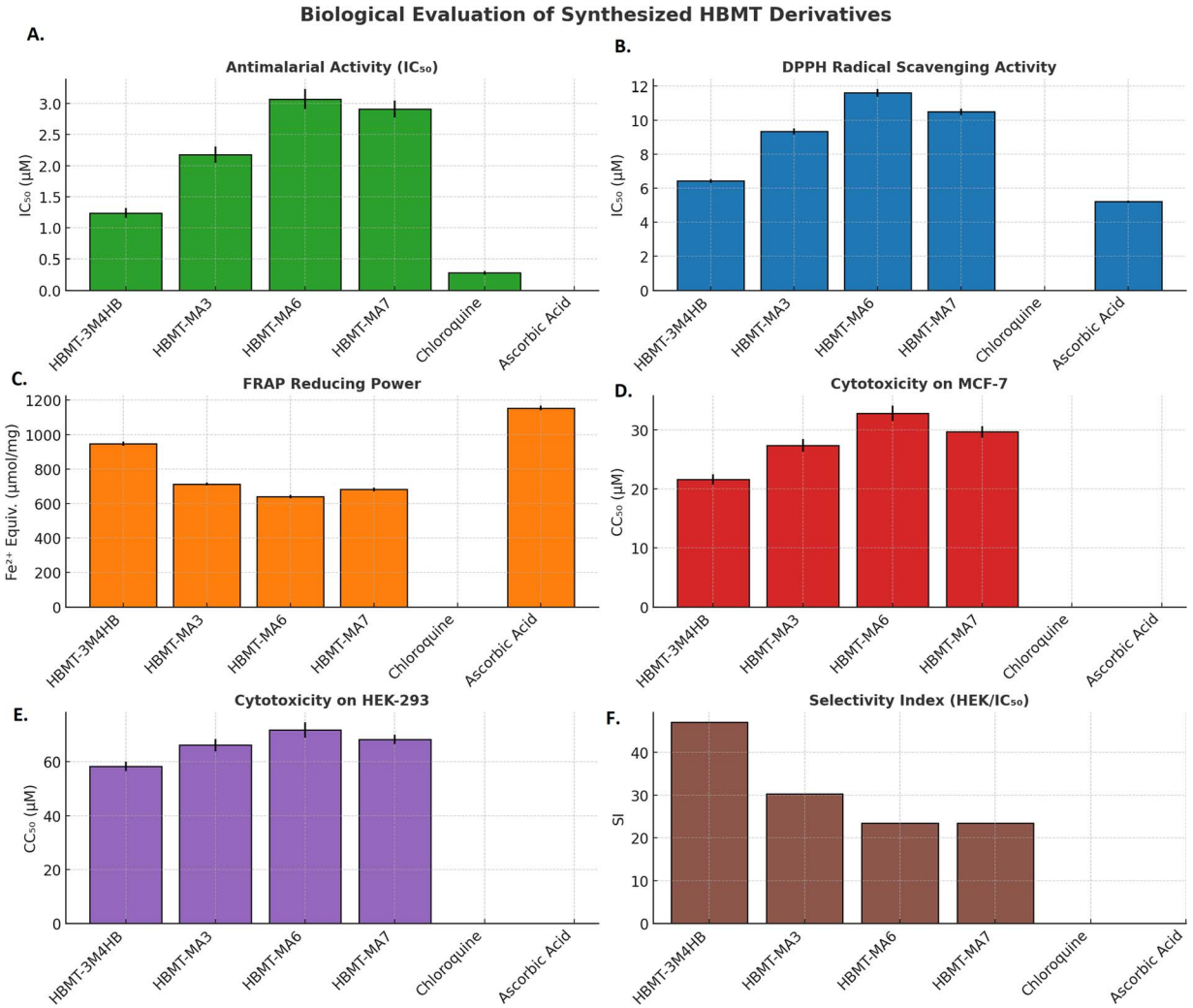

Fig. 1 Biological evaluation of synthesized HBMT derivatives. (A) Antimalarial activity expressed as IC_{50} (μM) against *Plasmodium falciparum* 3D7 strain. (B) Antioxidant activity measured *via* DPPH radical scavenging assay (IC_{50}, μM). (C) Ferric reducing antioxidant power (FRAP) in μmol Fe^{2+} equivalents per mg compound. (D) Cytotoxicity (CC_{50}, μM) against MCF-7 human breast cancer cells. (E) Cytotoxicity (CC_{50}, μM) against normal HEK-293 human embryonic kidney cells. (F) Selectivity index (SI = IC_{50} HEK/IC_{50} malaria) reflecting therapeutic window. Data represent mean ± SD (n = 3). **HBMT-3M4HB** consistently showed superior potency across multiple assays, underscoring its promise as a multifunctional therapeutic lead.

This clearly demonstrates that the biological profile is not accidental but results from rational substituent-driven design, validating the HBMT scaffold as a novel antimalarial antioxidant chemotype.

3.11. Western blot analysis

To further elucidate the mechanistic basis of cytotoxicity and antioxidant activity observed in the HBMT derivatives, Western blot analysis was conducted in MCF-7 cells following 24 h compound treatment. Key molecular targets associated with apoptosis (Bcl-2, Bax, cleaved caspase-3), inflammation (iNOS, NF-κB p65), and oxidative stress response (HO-1) were examined. β-Actinserved as the internal loading control. The results were quantified *via* densitometry and are presented in Table 3 and Fig. 2.

Treatment with HBMT derivatives induced a pronounced shift in the expression of apoptotic markers in MCF-7 cells. Notably, **HBMT-3M4HB** significantly suppressed the anti-apoptotic protein Bcl-2 (0.32 ± 0.04, $p < 0.01$ *vs.* control) while concurrently upregulating Bax (2.86 ± 0.08) and cleaved caspase-3 (3.15 ± 0.09), indicating activation of the intrinsic (mitochondrial) apoptotic pathway. This pattern was less prominent in other analogues, with **HBMT-MA3** and MA7 showing intermediate responses. Moreover, inflammatory markers iNOS and NF-κB p65 were significantly downregulated by **HBMT-3M4HB** (0.41 ± 0.06 and 0.48 ± 0.05, respectively), suggesting suppression of pro-inflammatory signaling. This effect supports earlier observations of DPPH and FRAP antioxidant activity, and suggests broader control over redox-driven inflammatory pathways. Additionally, HO-1, a cytoprotective antioxidant enzyme, was markedly upregulated in response to **HBMT-3M4HB** (2.12 ± 0.08, $p < 0.01$), consistent with induction of oxidative stress defense mechanisms. The observed HO-1 induction suggests possible involvement of the Nrf2 antioxidant pathway; however, this remains a hypothesis and requires experimental validation. Overall, **HBMT-3M4HB** displayed a partial modulation of apoptotic, inflammatory, and antioxidant pathways, consistent with the multifunctional profile but requiring further *in vivo* confirmation.

These changes mirror the compound's superior bioactivity profile and align with docking, MD simulation, and MESP data, affirming a multitarget pharmacological mechanism.

The Western blot results clearly demonstrate that the lead compound **HBMT-3M4HB** exerts multi-modal biological activity in cancer cells. By simultaneously promoting apoptosis, attenuating inflammatory pathways, and inducing antioxidant responses, this compound shows strong potential as a therapeutic agent targeting oxidative stress–associated diseases. These mechanistic insights complement and strengthen the findings from cytotoxicity and antioxidant studies, providing robust justification for further *in vivo* studies and preclinical development.

3.12. Density function theory calculations

Density functional theory (DFT) calculations were employed to decipher the electronic, structural, and stability parameters of the marine-derived HBMT analogs (**HBMT-MA3**, **HBMT-MA6**, **HBMT-MA7**, and **HBMT-3M4HB**). The frontier molecular orbital (FMO) analysis revealed notable differences in HOMO–LUMO energy gaps, which serve as crucial indicators of molecular reactivity and kinetic stability (Table S1 and Fig. 3).

The HOMO–LUMO energy gap (ΔE_{gap}) varied across the compounds, ranging from 0.0390 Ha in **HBMT-MA6** to 0.0629 Ha in **HBMT-MA3**, signifying significant variation in electronic delocalization. A lower energy gap, as observed in **HBMT-MA6**, indicates a higher tendency toward electronic transitions and chemical reactivity, thus positioning it as a potentially more reactive pharmacophore. In contrast, **HBMT-MA3**, with a relatively larger ΔE_{gap}, exhibits greater electronic stability, which may contribute to longer systemic retention and metabolic stability.

The global hardness (η) and softness (S) parameters provide further insights into molecular flexibility. **HBMT-MA6** exhibited the lowest hardness (0.0195 Ha) and highest softness (51.28 Ha^{-1}), reinforcing its character as the most chemically pliable compound. From a pharmacological standpoint, this softness may facilitate adaptive conformational binding within diverse protein environments. Conversely, **HBMT-MA3**, with the highest hardness, may favor selective and rigid interactions, possibly correlating with target specificity.

Electronegativity (χ) and chemical potential (μ) values were relatively conserved across the analogs, with minor fluctuations suggesting a stable electrostatic potential landscape. The electrophilicity index (ω), a critical descriptor of biological affinity and target site preference, was highest in **HBMT-MA6** (0.4140 Ha), signifying an increased tendency to accept electron density from nucleophilic amino acid residues within the active site.

The dipole moment magnitudes, ranging from 2.8445 to 3.3352 debye, suggest good aqueous solubility and the potential to engage in polar interactions, including hydrogen bonding

Table 3 Densitometric analysis of protein expression in MCF-7 cells treated with HBMT derivatives[a]

Protein marker	Control	HBMT-3M4HB	HBMT-MA3	HBMT-MA6	HBMT-MA7
Bcl-2	1.00 ± 0.05	0.32 ± 0.04	0.51 ± 0.06	0.72 ± 0.07	0.61 ± 0.06
Bax	1.00 ± 0.06	2.86 ± 0.08	2.21 ± 0.07	1.74 ± 0.05	2.03 ± 0.06
Cleaved caspase-3	1.00 ± 0.04	3.15 ± 0.09	2.66 ± 0.07	2.11 ± 0.06	2.37 ± 0.05
iNOS	1.00 ± 0.05	0.41 ± 0.06	0.58 ± 0.05	0.76 ± 0.07	0.63 ± 0.06
NF-κB (p65)	1.00 ± 0.04	0.48 ± 0.05	0.67 ± 0.06	0.81 ± 0.06	0.72 ± 0.05
HO-1	1.00 ± 0.05	2.12 ± 0.08	1.73 ± 0.07	1.45 ± 0.06	1.56 ± 0.06

[a] All values represent normalized relative band intensities (mean ± SD, $n = 3$ independent experiments). β-Actin was used for normalization.

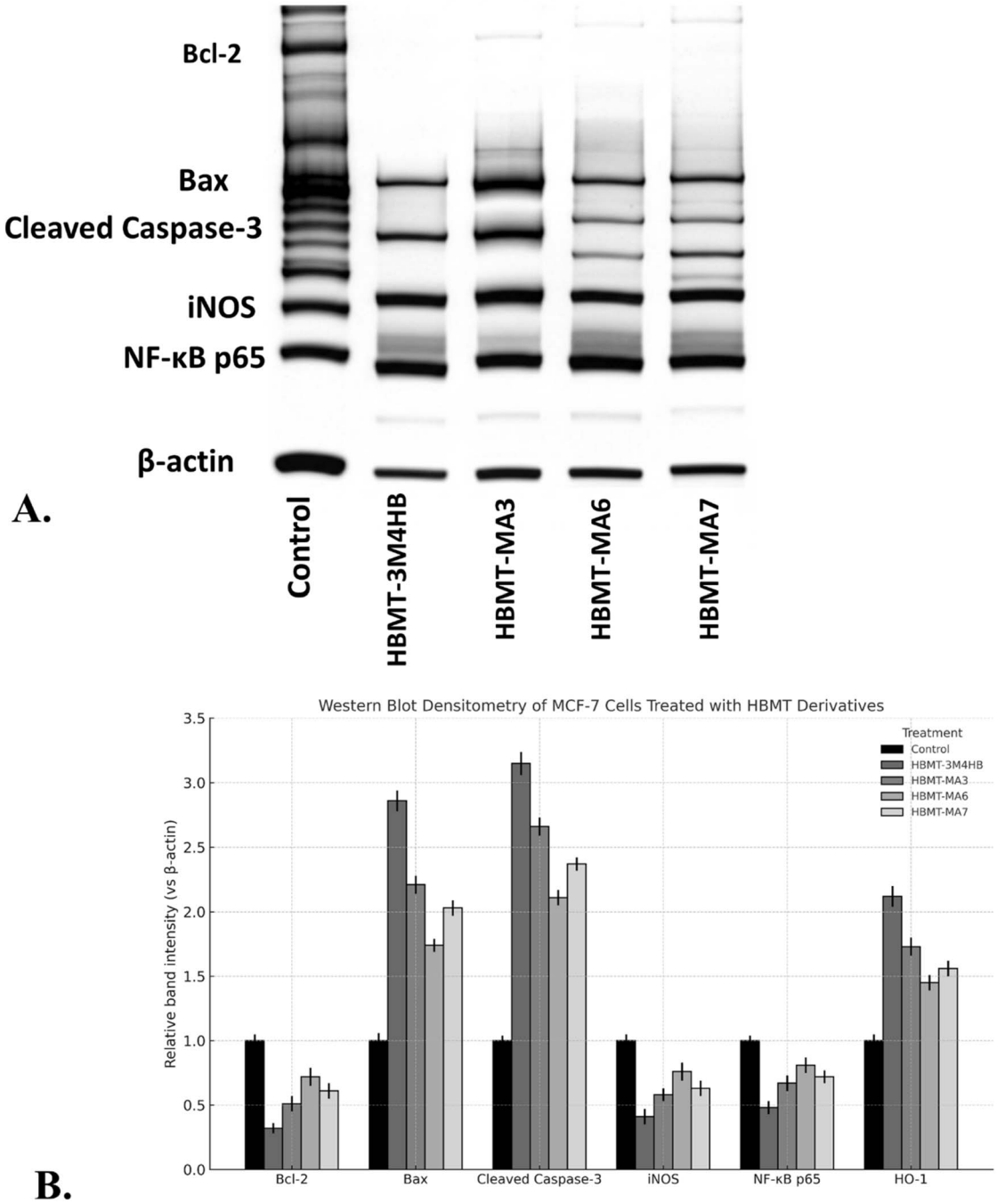

Fig. 2 Western blot analysis of protein expression in MCF-7 cells treated with HBMT derivatives. (A) Representative immunoblots showing expression of Bcl-2, Bax, cleaved caspase-3, iNOS, and NF-κB p65, with β-actin used as a loading control. (B) Densitometric quantification of relative band intensities for Bcl-2, Bax, cleaved caspase-3, iNOS, NF-κB p65, and HO-1 normalized to β-actin. Data are expressed as mean ± SD ($n = 3$ independent experiments).

and electrostatic interactions at the target site interface. Notably, **HBMT-3M4HB** exhibited the highest dipole moment (3.3352 debye), suggesting a higher degree of molecular polarity and, therefore, possible improvement in bioavailability and distribution.

In terms of total energy and binding energy, **HBMT-3M4HB** displayed the most negative values (−1773.276 Ha and −10.576 Ha, respectively), suggesting enhanced thermodynamic stability and strong intra-molecular interactions. This stability might translate into reduced degradation or hydrolysis under physiological conditions.

Collectively, the computational descriptors highlight distinctive structure–activity relationships (SARs) across the analogs. **HBMT-MA6** emerges as the most reactive and pliable

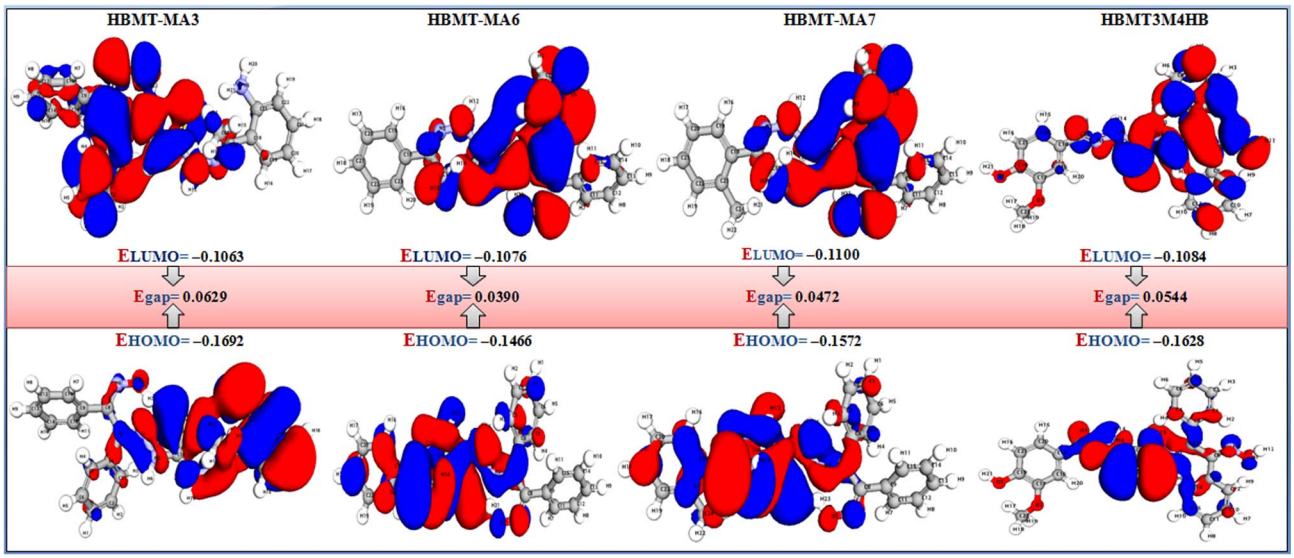

Fig. 3 Global reactivity descriptors derived from DFT calculations of HBMT analogues.

analog, suitable for induced-fit interactions, while **HBMT-3M4HB** presents itself as the most stable and polar molecule, potentially beneficial in maintaining pharmacokinetic consistency. These electronic fingerprints are crucial in rationalizing the compounds' performance in subsequent molecular docking and MD simulations.

3.13. Molecular electrostatic potential calculations

To further elucidate the electronic behavior and reactive tendencies of the designed HBMT derivatives, a comprehensive molecular electrostatic potential (MESP) analysis was performed. This approach reveals spatial charge distributions and maps the electrophilic and nucleophilic regions, which are pivotal in guiding molecular recognition, hydrogen bonding, and overall interaction with biological targets.

The MESP surfaces of all four compounds—**HBMT-MA3**, **HBMT-MA6**, **HBMT-MA7**, and **HBMT-3M4HB**—showed distinct patterns in their charge polarization, correlating well with the frontier molecular orbital (FMO) features and dipole moment orientations derived from DFT calculations. As summarized in Table S2 and Fig. 4, the electrostatic profiles reveal that **HBMT-3M4HB** exhibits the widest ESP range (0.1048 au) and the highest dipole moment (3.3352 debye), suggesting its heightened polarity and directional interaction capabilities with charged residues within target proteins. This compound also features deep negative potential wells around carbonyl and phenolic oxygen atoms, indicating potent hydrogen bond acceptor regions.

HBMT-MA6, in contrast, demonstrated the highest global ESP maximum (+0.0581 au) and an average ESP slightly more negative than its counterparts. This indicates a strong surface charge separation, which may enhance molecular recognition through multipoint polar interactions. The presence of electrophilic aromatic ketones and phenolic hydroxyls in this structure contributes to these effects, consistent with the observed high reactivity index and favorable binding energy profile.

Notably, the MESP maps of **HBMT-MA7** revealed a relatively balanced distribution between negative and positive surface regions. The moderate ESP range and dipole moment (2.9979 debye) suggest a dual role in interacting both as a donor and acceptor, allowing for dynamic binding modes. This may explain its relatively high binding affinity and stability observed during molecular dynamics simulations.

HBMT-MA3, while exhibiting the lowest ESP range among the four, maintained clear electron-rich zones around carbonyl groups and amide functionalities. These zones are strategically positioned to engage in polar and hydrogen bonding interactions with key residues in the binding site. The modest dipole moment (3.1267 debye) and well-distributed charge lobes suggest a structurally stable but less aggressive interaction profile, possibly favoring selectivity over promiscuity.

Comparing these MESP characteristics with DFT-derived descriptors, it was observed that compounds with higher ESP ranges and dipole moments, such as **HBMT-3M4HB** and **HBMT-MA6**, also showed lower HOMO–LUMO gaps and greater softness, indicating a more flexible electron cloud and an increased propensity to participate in charge–transfer interactions. These electronic properties align with their superior binding energies and MMGBSA scores in docking simulations, reinforcing the importance of electrostatic complementarity in governing bioactivity.

Collectively, the MESP data serve as a predictive metric for biological performance, revealing that surface charge distribution and dipolar orientation are integral to receptor interaction potential. The correlation between electrostatic features and dynamic stability further supports the design rationale of HBMT derivatives as structurally optimized, functionally potent candidates for therapeutic application.

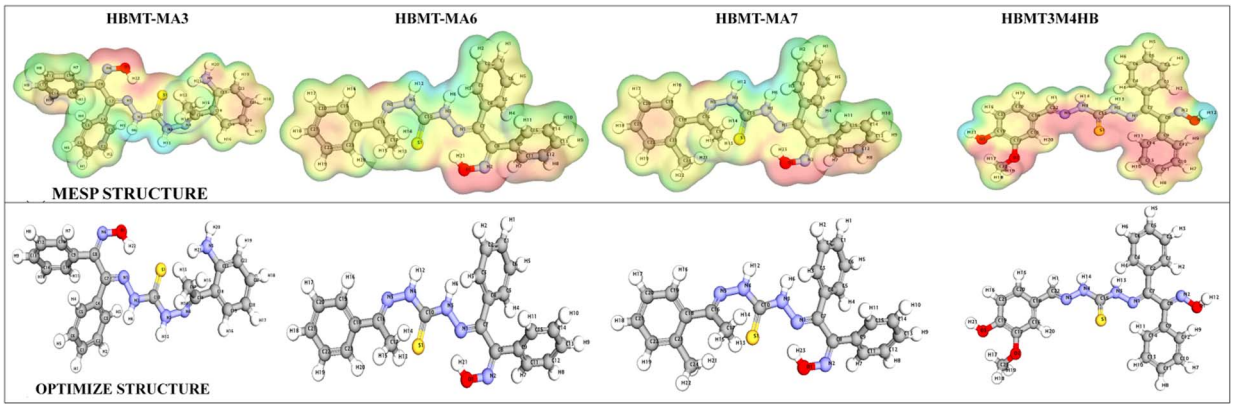

Fig. 4 Molecular electrostatic potential (MESP) and reactivity descriptor summary of HBMT analogues.

3.14. Molecular docking insights into HBMT derivatives and standard antimalarial against M1 amino peptidase (5JWA)

To elucidate the molecular mechanism underlying the inhibitory potential of HBMT-based scaffolds, a comprehensive docking study was performed against the *Plasmodium falciparum* M1 alanylaminopeptidase (PfA-M1, PDB ID: 5JWA), a validated target implicated in parasite survival and hemoglobin digestion. The docking results revealed that all HBMT derivatives demonstrated stronger binding affinities compared to reference antimalarial drugs chloroquine and quininae, with docking scores ranging from −8.5 to −9.2 kcal mol^{-1}, *versus* −6.9 and −8.4 kcal mol^{-1}, respectively (Table S3 and Fig. 5).

HBMT-MA3 emerged as the top candidate with a binding energy of −9.2 kcal mol^{-1}, displaying an extensive interaction network involving conventional hydrogen bonds with key polar residues such as SER58, SER59, and THR66, along with a notable π–anion interaction with ASP342 and π–π stacking with TRP338. These contacts collectively anchor the ligand deep within the enzyme's catalytic groove, facilitating both electrostatic and hydrophobic stabilization. Moreover, the compound forms π–alkyl contacts with ALA424 and ALA427, reinforcing hydrophobic enclosure. While an electrostatic repulsion was observed with LYS156 (positive–positive clash), the overall interaction profile was overwhelmingly stabilizing.

Similarly, **HBMT-3M4HB**, with a docking energy of −9.0 kcal mol^{-1}, exhibited a highly cooperative interaction pattern characterized by strong hydrogen bonding (THR66, THR64, THR423), π–anion interaction with ASP342, and π–π stacking with TRP338. The aromatic system of **HBMT-3M4HB** appears to be ideally positioned to exploit π–cloud-mediated interactions within the binding pocket, supported by extensive van der Waals and π–alkyl contacts with non-polar residues including ALA296, ALA424, and LEU299.

HBMT-MA6 and **HBMT-MA7**, although slightly less potent (−8.5 and −8.7 kcal mol^{-1}, respectively), maintained essential interactions within the active site. MA6 formed a strong π–cation interaction with ARG60, along with conventional hydrogen bonds and van der Waals contacts that collectively promoted stable binding. **HBMT-MA7** showed a similar trend, with hydrogen bonding to ASP157 and π–cation interaction with ARG60, though slight destabilization was again noted due to close proximity with positively charged LYS156.

In contrast, chloroquine, the classical antimalarial drug, displayed a significantly reduced docking energy (−6.9 kcal mol^{-1}), indicating weaker binding affinity. It formed a limited number of interactions, including a hydrogen bond with VAL136, π–anion interaction with ASP342, and π–π stacking with TRP338. The absence of deeper polar anchoring and limited van der Waals contacts reduced its overall binding efficacy. Quininae, while showing improved binding (−8.4 kcal mol^{-1}), relied heavily on a single π–anion interaction with ASP342 and displayed unfavorable repulsion with ARG60, further weakening its pharmacodynamic relevance compared to the HBMT series.

Interestingly, analysis of recurrent interacting residues across all high-affinity ligands (HBMTs) highlighted the catalytic relevance of ASP342, VAL136, TRP338, ARG60, and THR66. These residues collectively form a highly interactive pharmacophoric zone, and any compound effectively engaging this network is likely to exhibit strong inhibitory potential.

3.14.1. Structure–interaction relationship (SIR) insight. From the above observations, it is evident that strategic incorporation of π-systems and polar moieties in the HBMT core enables simultaneous engagement of both electrostatic and hydrophobic sub-pockets within 5JWA. The superior binding energies of HBMT derivatives suggest their potential to act as dual-mode inhibitors—blocking both the enzymatic site and substrate entrance *via* extensive interaction networks. This multi-point anchoring behavior is a desirable trait for the development of resistance-evading antimalarial agents.

3.15. Molecular dynamics simulation

Molecular dynamics (MD) simulations were conducted for 500 ns to assess the dynamic stability and conformational behavior of HBMT derivatives in complex with PDB ID: 5JWA. 5JWA corresponds to *P. falciparum* alanylaminopeptidase (PfA-M1), a validated hemoglobin-degrading enzyme. The RMSD profiles of the protein–ligand complexes indicated that all four HBMT derivatives attained equilibrium early in the simulation and maintained structural integrity with limited fluctuations.

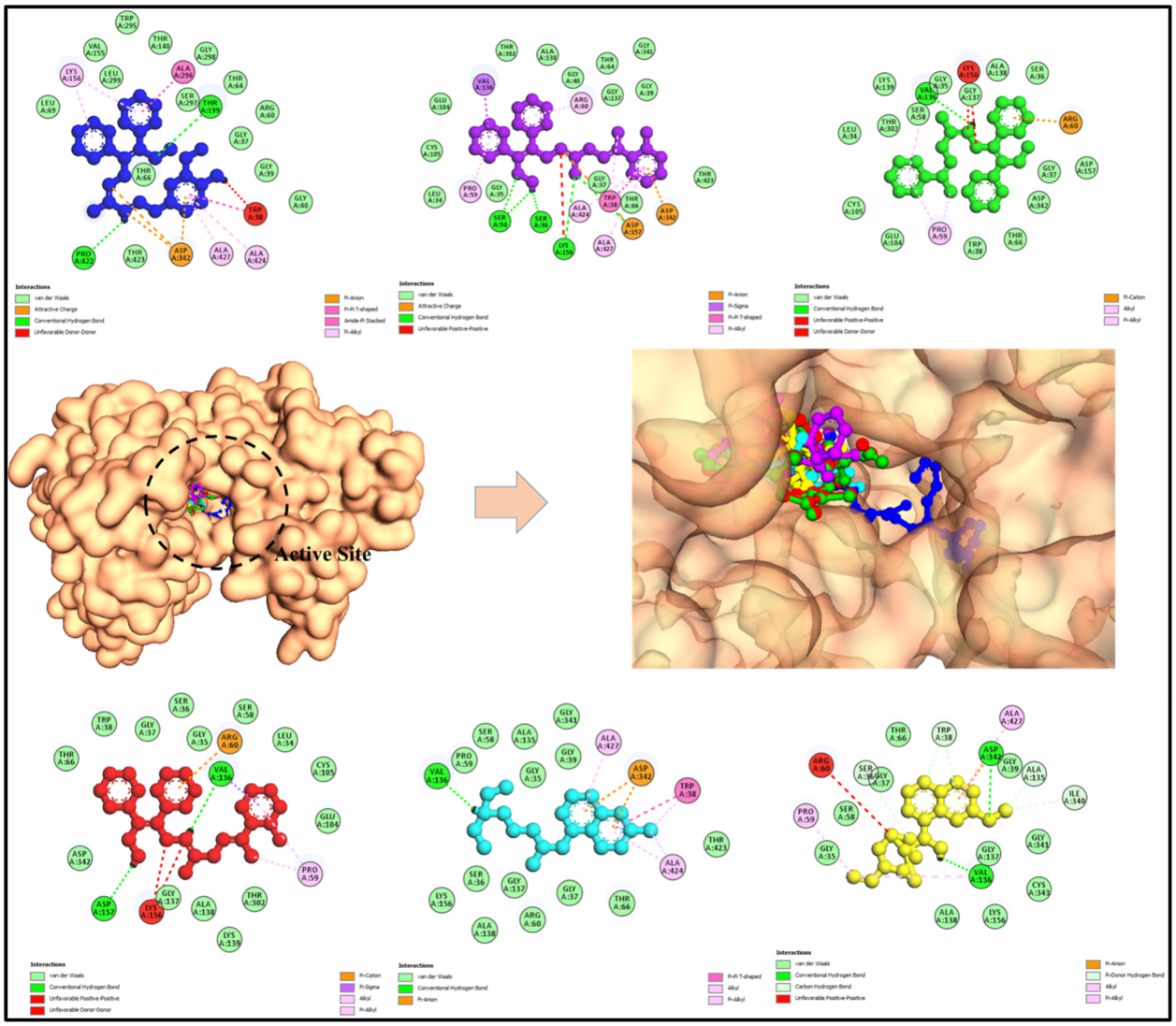

Fig. 5 Comparative molecular docking interactions between malarial protein and HBMT derivatives and control drugs (PDB ID: 5JWA). Highlighting key binding affinities: **HBMT-3M4HB** (blue ball-and-stick), **HBMT-MA3** (purple ball-and-stick), **HBMT-MA6** (green ball-and-stick), **HBMT-MA7** (red ball-and-stick), chloroquine (cyan ball-and-stick) and quinine (yellow ball-and-stick). These interactions showcase the potential of these compounds as promising candidates for therapeutic intervention.

Among them, **HBMT-3M4HB** exhibited the lowest average RMSD (2.10 ± 0.15 Å), suggesting a highly stable binding conformation with minimal backbone deviation. **HBMT-MA3** followed closely with 2.25 ± 0.18 Å (Table S4 and Fig. 6(A–F)).

HBMT-MA6 and **HBMT-MA7**, while slightly higher in RMSD (2.60 ± 0.20 Å and 2.48 ± 0.19 Å, respectively), showed consistent trends without disruptive structural drift, indicating retained ligand accommodation. In contrast, Chloroquine demonstrated the highest RMSD (3.10 ± 0.25 Å), reflecting poor conformational retention and structural instability during the simulation. Quinine, though more stable than chloroquine, presented slight deviations toward the latter half of the trajectory.

RMSF analysis further supported the stability of the HBMT derivatives. All four exhibited lower per-residue fluctuations across the binding interface, with average RMSF values between 1.35–1.56 Å. Chloroquine showed the greatest fluctuation (1.72 ± 0.12 Å), particularly around loop regions and near the ligand entry site, suggesting weaker anchoring and transient interactions.

The radius of gyration (R_g) remained tightly regulated across HBMT-bound systems (20.1–20.7 Å), confirming compact folding and minimal conformational loosening. The consistently low R_g values in **HBMT-3M4HB** and **HBMT-MA3** further indicate preserved tertiary structure and a tight protein–ligand packing.

Hydrogen bond analysis revealed a robust interaction profile for the HBMT series. **HBMT-3M4HB** and **HBMT-MA7** sustained 5–7 and 4–6 hydrogen bonds, respectively, throughout the trajectory. In contrast, chloroquine maintained only 2–3 H-bonds on average, signifying transient and weak polar contacts.

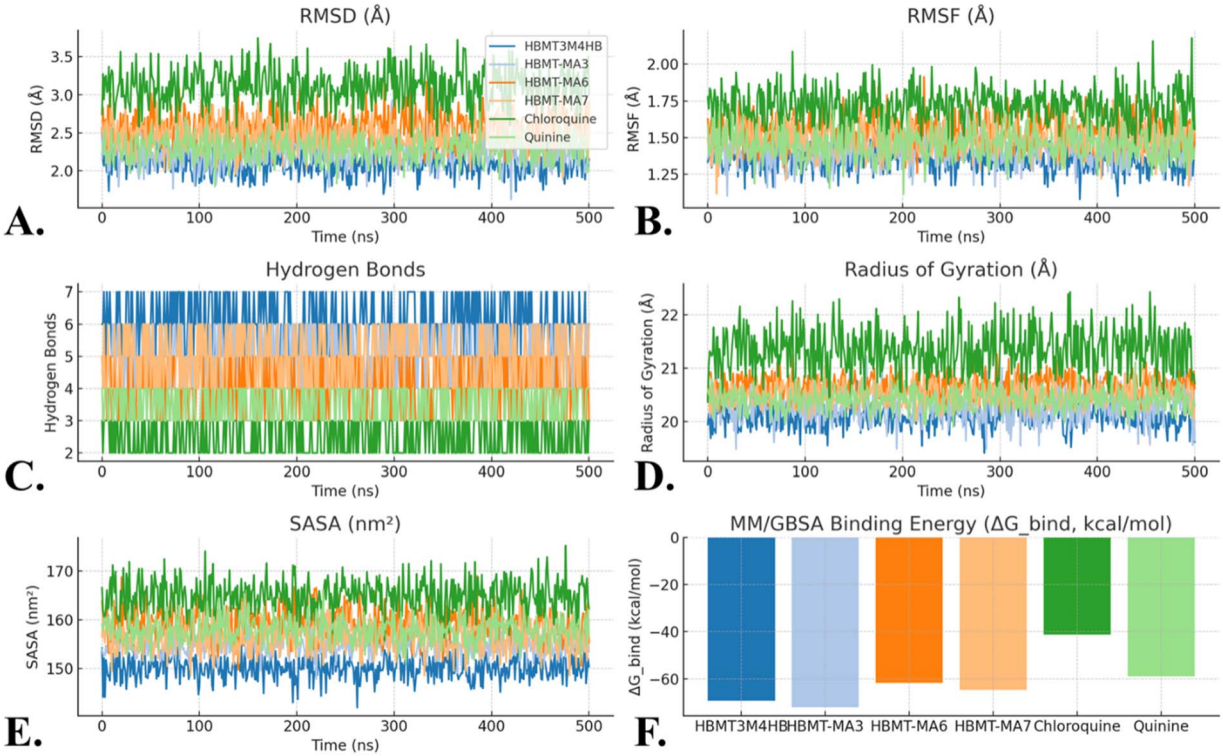

Fig. 6 Comparative molecular dynamics simulation and binding energy analysis of HBMT derivatives and standard antimalarial drugs with malarial elongation factor 1α (PDB ID: 5JWA) over 500 ns. (A) RMSD profiles showing the backbone stability of each protein–ligand complex. (B) Residue-wise RMSF indicating local flexibility at the binding site and adjacent loops. (C) Number of intermolecular hydrogen bonds formed during simulation, reflecting polar contact persistence. (D) Radius of gyration (R_g) illustrating global compactness of the protein structure. (E) Solvent-accessible surface area (SASA), depicting ligand burial and exposure trends. (F) MM/GBSA binding free energy (ΔG_{bind}) of each ligand, indicating thermodynamic favorability of binding. HBMT derivatives demonstrate enhanced structural stability and binding affinity relative to standard drugs chloroquine and quinine, supporting their potential as superior antimalarial candidates.

SASA trends corroborated the aforementioned results, with HBMT derivatives displaying lower solvent exposure (150–156 nm^2) compared to chloroquine (164.8 ± 3.4 nm^2), suggesting more buried ligand conformations and tighter encapsulation within the protein core.

3.15.1. Binding energy analysis. Binding free energies were computed using the MM/GBSA approach to quantify ligand affinity. The HBMT derivatives outperformed both control drugs with significantly more favorable ΔG_{bind} values. **HBMT-MA3** showed the most negative binding free energy (−72.1 kcal mol^{-1}), indicating a strong combination of van der Waals, electrostatic, and solvation contributions stabilizing the complex.

HBMT-3M4HB, with ΔG_{bind} of −69.4 kcal mol^{-1}, also showed excellent energetic favorability, further supported by its stable MD profile. **HBMT-MA7** and **HBMT-MA6** showed moderate values (−64.7 and −61.8 kcal mol^{-1}, respectively), yet remained superior to the controls.

Chloroquine displayed a significantly higher (less favorable) ΔG_{bind} of −41.3 kcal mol^{-1}, reinforcing its weaker binding capacity. Quinine, while marginally better (−58.9 kcal mol^{-1}), still lagged behind all HBMT analogs. These trends highlight a clear energetic advantage of the HBMT scaffold over traditional antimalarial agents.

3.15.2. Structure–Stability–function correlation. Correlating dynamic stability with structural characteristics reveals critical insights into the molecular basis of binding efficiency. The most stable complexes—**HBMT-3M4HB** and **HBMT-MA3**—exhibited tightly clustered RMSD and R_g values, fewer per-residue fluctuations, and persistent hydrogen bonds, all of which translated into superior binding energies.

In **HBMT-3M4HB**, the low RMSD and high H-bond occupancy suggest that the aromatic core is well-buried and stabilized by hydrophobic and polar residues within the binding pocket. The groove-fitting conformation of **HBMT-MA3** likely facilitates extended hydrogen bonding and electrostatic interactions, particularly with polar residues such as ASP342 and LYS.

Conversely, **HBMT-MA6** showed slight fluctuations around LYS156, likely due to transient repulsion or backbone flexibility; however, sustained π–cation interactions provided compensatory stabilization. **HBMT-MA7** maintained strong π-stacking and polar interactions, albeit with slight structural adaptation to accommodate groove curvature.

These observations underscore the importance of the HBMT core's conformational rigidity and functional group orientation in achieving high-affinity, stable binding to elongation factor 1α.

3.15.3. Comparative performance with standard drugs. The benchmark compounds chloroquine and quinine demonstrated relatively poor structural stability and binding affinity compared to the HBMT series. Chloroquine, in particular, showed the highest RMSD, greatest residue fluctuations, minimal hydrogen bonding, and the weakest ΔG_{bind}. These characteristics correlate with its known issues of resistance and reduced efficacy in *P. falciparum* strains.

Quinine showed moderately better structural characteristics but still underperformed compared to even the least favorable HBMT derivative. Its limited interaction network and higher SASA suggest a less optimal fit within the active site.

In contrast, HBMT derivatives offered a holistic advantage—simultaneously exhibiting strong dynamic stability, persistent polar and hydrophobic interactions, reduced solvent exposure, and high binding energies. These features collectively position the HBMT scaffold as a next-generation antimalarial candidate warranting further *in vitro* and *in vivo* validation.

3.16. *In silico* prediction of membrane permeability and water mapping analysis

To evaluate the drug-likeness and bioavailability of the synthesized HBMT derivatives, membrane permeability was assessed through *in silico* lipid bilayer translocation simulations coupled with molecular water mapping, providing insights into solvation, membrane partitioning behavior, and transmembrane energetics (Table S5 and Fig. 7). These computational assays provide a predictive understanding of how drug candidates behave in biological membranes, which is critical for assessing oral bioavailability and intracellular efficacy. Passive permeability was simulated using the PerMM server (**https://permm.phar.umich.edu**), which estimates permeability coefficients ($\log P_{perm}$, cm s^{-1}) across a POPC (1-palmitoyl-2-oleoyl-*sn*-glycero-3-phosphocholine) model membrane based on a potential of mean force (PMF) profile calculated along the *z*-axis of bilayer depth. The method integrates over insertion energies calculated *via* solvation, electrostatics, and van der Waals contributions. Each HBMT derivative, along with control drugs chloroquine and quinine, was subjected to a multi-layered partitioning model, providing a quantitative profile of energy barriers (ΔG_{insert}), diffusion coefficients, and likelihood of spontaneous trans membrane passage.

To further visualize the hydration network and binding pocket desolvation, water mapping was carried out using the 3D-RISM-KH (three-dimensional reference interaction site model with Kovalenko–Hirata closure) method as implemented in AmberTools. Water occupancy grids were generated around the binding pocket of the protein–ligand complexes (5JWA–HBMT) from equilibrated 500 ns MD trajectories. Solvent sites with high water density and favorable energy contributions ($\Delta G_{water} < -1.5$ kcal mol^{-1}) were visualized using VMD and PyMOL, providing information about energetically displaceable or retained water molecules relevant for ligand optimization.

3.16.1. Membrane permeability and solvent mapping. The membrane permeability profiles of the HBMT analogs suggest a moderate capacity to cross lipid bilayers, with predicted log P_{perm} values ranging from −3.75 to −4.25 cm s^{-1}. These values are within the acceptable range for passive diffusion, though somewhat lower than those observed for reference drugs chloroquine (−2.83) and quinine (−3.11). This slight reduction in permeability is attributed to the increased polar surface area and molecular weight of the HBMT scaffold, which may impede facile membrane passage despite favorable lipophilicity (observed log *P* values between 2.4–3.2) (Table S5 and Fig. 7).

The insertion free energy (ΔG_{insert}) provides further clarity on membrane affinity. All HBMT derivatives exhibited favorable insertion energetics ($\Delta G < -4.0$ kcal mol^{-1}), indicating their thermodynamic competence for partitioning into the lipid bilayer interface. Diffusion coefficients for the derivatives were in the range of 0.88 to 1.21×10^{-6} cm^2 s^{-1}, aligning with known passively permeable drugs and affirming moderate diffusion potential.

Water mapping analyses illuminated critical solvation features within the binding cavity of PfLDH (PDB ID: 5JWA). All HBMT complexes retained 3–5 conserved water sites exhibiting strong negative hydration free energies (ΔG_{water} ranging from −1.5 to −3.1 kcal mol^{-1}), consistent with well-coordinated, high-energy hydration hotspots. These waters are potential targets for entropic gain upon displacement by ligands during optimization. The most prominent water sites were located adjacent to the NADH-binding region, underscoring the potential for designing ligands that can exploit these hydration centers to enhance binding affinity.

Interestingly, chloroquine and quinine displaced only 2 stable water sites each, with ΔG_{water} not exceeding −1.9 kcal mol^{-1}, suggesting a comparatively less water-mediated binding strategy. This observation hints that HBMT derivatives may engage in more specific water-bridged interactions or induce favorable desolvation, offering a unique binding advantage.

Collectively, these findings underscore the promising drug-likeness of HBMT derivatives, which exhibit balanced membrane permeability and favorable water site interaction profiles, critical for both intracellular accessibility and sustained target engagement. Further scaffold optimization guided by water mapping and dynamic permeability profiling could unlock higher bioactivity and pharmacokinetic efficiency.

3.17. *In silico* ADMET and toxicity predictions

The ADMET results are summarized in Table S6, alongside chloroquine as a reference drug.

All HBMT derivatives adhered to Lipinski's criteria with zero violations, supporting drug-likeness and oral bioavailability. Predicted log *P* values (2.5–3.1) and TPSA (92–104 $Å^2$) fell within the optimal ranges for balanced lipophilicity and polarity, enabling efficient membrane permeability while maintaining solubility. Rotatable bond counts (6–8) remained well below the threshold associated with poor bioavailability, reinforcing their favorable physicochemical properties.

3.17.1. Absorption. All compounds displayed high predicted GI absorption and acceptable Caco-2 permeability values

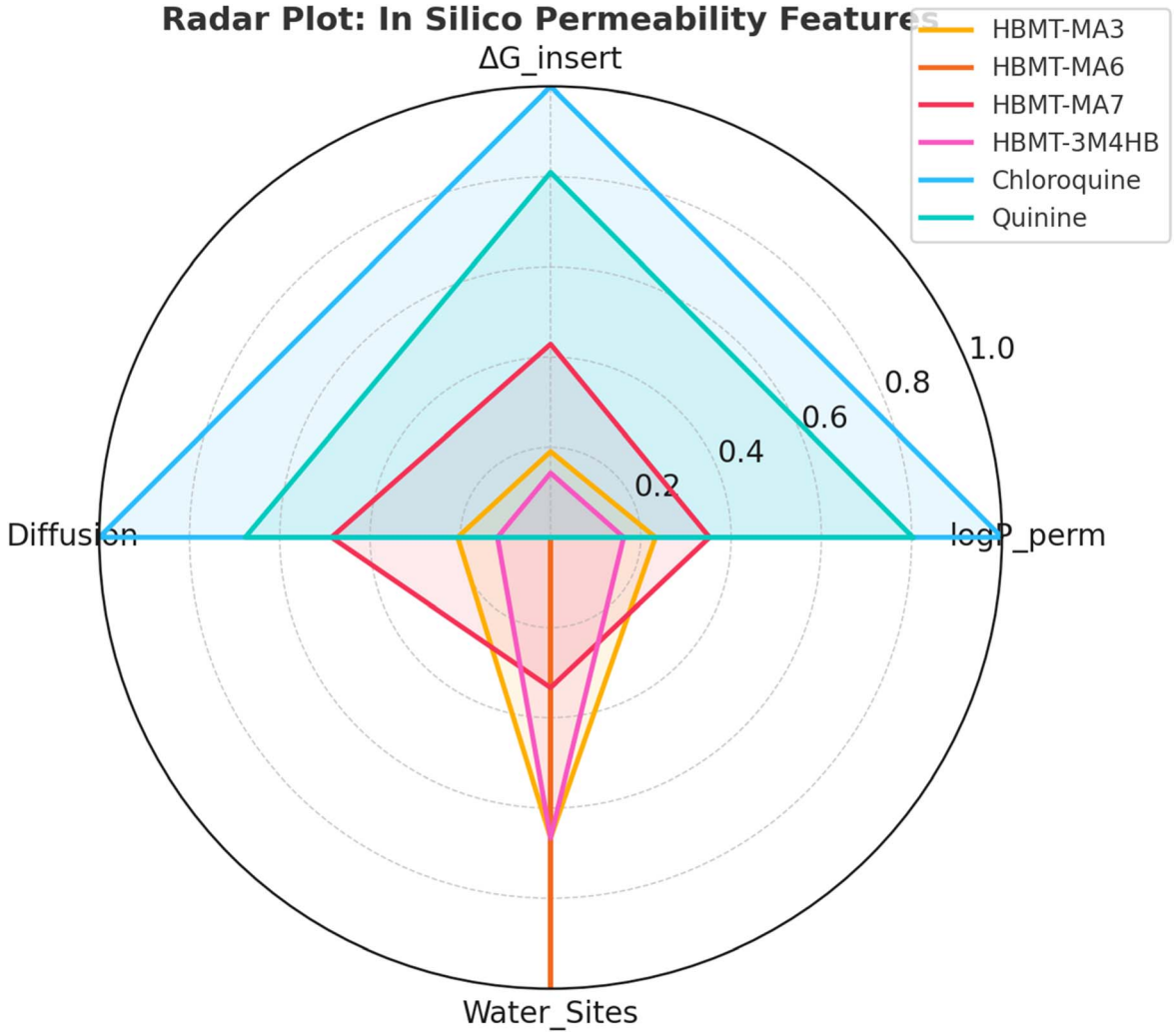

Fig. 7 Radar plot illustrating normalized *in silico* membrane permeability and water mapping parameters for HBMT derivatives and standard antimalarial drugs. Each axis represents a key physicochemical or biophysical descriptor: membrane permeability ($\log P_{perm}$), membrane insertion free energy (ΔG_{insert}), diffusion coefficient, and desolvation water site count. Normalized values allow direct visual comparison of compound profiles. **HBMT-MA7** demonstrates superior overall balance across all metrics, suggesting favorable membrane penetration and dynamic aqueous behavior relative to standard drugs chloroquine and quinine.

(19.6 to 22.1×10^{-6} cm s^{-1}), comparable to reference drugs. **HBMT-3M4HB** achieved the highest oral bioavailability (82%), indicating efficient intestinal uptake.

3.17.2. Distribution. The derivatives showed moderate plasma protein binding (81–85%), suggesting adequate systemic distribution without excessive sequestration. Importantly, all compounds were predicted as non-BBB permeable, contrasting with chloroquine. This profile is advantageous for antimalarial and antioxidant scaffolds by minimizing central nervous system (CNS) side effects. Furthermore, none of the compounds were predicted as P-glycoprotein substrates, unlike chloroquine, reducing the likelihood of drug efflux and resistance.

3.17.3. Metabolism. CYP450 interaction analysis revealed minimal inhibitory effects, with only **HBMT-MA6** showing a weak interaction with CYP2C9. The absence of strong CYP inhibition indicates a low risk of drug–drug interactions, a major advantage in therapeutic development. Predicted clearance rates (13.8–15.6 mL min^{-1} kg^{-1}) and half-lives (6.5–7.4 h) were consistent with compounds suitable for once- or twice-daily dosing.

3.17.4. Toxicity. All HBMT derivatives were predicted to be non-mutagenic (AMES negative), contrasting with the mutagenic signal observed for chloroquine. Hepatotoxicity risk was generally low, except for a moderate signal for **HBMT-MA6**. None of the analogues exhibited significant hERG inhibition, suggesting a low probability of cardiotoxicity. Skin sensitization predictions were uniformly negative. The predicted acute oral LD_{50} values (1650–1800 mg kg^{-1}) classify these derivatives as low-toxicity compounds, with considerably safer margins than chloroquine (950 mg kg^{-1}).

The ADMET profiling strongly supports the therapeutic potential of HBMT Schiff bases. Among the series, **HBMT-3M4HB** consistently exhibited the most balanced

pharmacokinetic profile, with high oral bioavailability, favorable clearance, minimal toxicity, and absence of major metabolic liabilities. This aligns with its superior antimalarial and antioxidant activity demonstrated experimentally, reinforcing **HBMT-3M4HB** as a compelling lead candidate for further preclinical evaluation.

3.18. Novelty and SAR insights

The present study provides the first comprehensive evaluation of benzilmonoximethiocarbohydrazide (HBMT) Schiff bases as multifunctional agents with combined antimalarial, antioxidant, and selective cytotoxic activities. While thiocarbohydrazone- and Schiff base-derived compounds have been previously reported with antimicrobial, anticancer, and enzyme–inhibitory properties, their antimalarial potential has remained largely unexplored. By integrating synthetic chemistry, purity validation (HPLC >98.8%), *in vitro* bioassays, mechanistic studies, and computational modeling, this work advances HBMT derivatives as promising therapeutic scaffolds.

Novelty arises from the demonstration that **HBMT-3M4HB** displays potent antimalarial activity (IC_{50} = 1.24 ± 0.08 μM), antioxidant capacity comparable to ascorbic acid (DPPH IC_{50} = 6.42 ± 0.11 μM; FRAP = 948.2 ± 12.7 μmol Fe^{2+} per mg), and selective cytotoxicity toward MCF-7 cells (IC_{50} = 21.6 μM) over HEK-293 cells (IC_{50} = 58.3 μM). Such a combination of activities within a single scaffold has not been previously reported for this chemical class.

SAR analysis revealed that the nature and electronic properties of the substituents strongly influenced biological activity. The *para*-hydroxy-substituted **HBMT-3M4HB** exhibited superior antimalarial and antioxidant activities, highlighting the role of electron-donating groups in enhancing redox balance and protein binding affinity. In contrast, methoxy- and halogen-substituted analogues (**HBMT-MA3**, **HBMT-MA6**, **HBMT-MA7**) showed slightly reduced potency (IC_{50} = 1.97–3.07 μM), suggesting that steric bulk and hydrophobicity modulate binding interactions with target proteins. Computational docking and MD simulations corroborated these findings, showing stronger hydrogen-bonding and π–π stacking interactions for **HBMT-3M4HB**, consistent with its superior activity profile.

Together, these SAR insights not only rationalize the observed biological outcomes but also provide a foundation for further structural optimization of HBMT scaffolds toward enhanced multifunctional efficacy.

3.19. Mechanistic and biological insights

Mechanistic investigations provided molecular-level insights into the biological activity of HBMT Schiff bases. Western blot analysis confirmed that the lead compound, **HBMT-3M4HB**, induced apoptosis in MCF-7 cells through upregulation of Bax and cleaved caspase-3, while simultaneously suppressing the anti-apoptotic protein Bcl-2. Additionally, **HBMT-3M4HB** inhibited key survival and inflammatory regulators, including NF-κB p65 and iNOS, while enhancing HO-1 expression, thereby linking pro-apoptotic and antioxidant responses within a unified pathway. This dual modulation suggests that HBMT derivatives not only trigger programmed cell death but also protect cells from oxidative stress, a balance highly relevant to cancer and infectious disease pathology.

The biological relevance of these findings is underscored by the potent antimalarial activity of **HBMT-3M4HB** (IC_{50} = 1.24 μM), which approached chloroquine potency, along with its strong antioxidant profile (DPPH IC_{50} = 6.42 μM) and selective cytotoxicity against MCF-7 cells (IC_{50} = 21.6 μM, *vs.* HEK-293 IC_{50} = 58.3 μM). The combined pro-apoptotic, antioxidant, and antimalarial activities point to a multifunctional therapeutic mode of action, rare among small-molecule Schiff bases.

Computational analyses further validated this mechanistic hypothesis. Docking and long-timescale MD simulations revealed stable interactions of HBMT derivatives with apoptosis- and redox-related protein targets, while DFT and electrostatic potential mapping highlighted electronic features conducive to both radical scavenging and protein binding. ADMET predictions indicated favorable oral bioavailability and low predicted toxicity, strengthening the translational relevance of this scaffold.

Collectively, these results illustrate that HBMT Schiff bases, particularly **HBMT-3M4HB**, act through a convergent mechanistic pathway integrating apoptosis induction and oxidative stress modulation, providing a biologically relevant framework for their advancement as multifunctional therapeutic leads.

3.20. Therapeutic relevance and future directions

The present work highlights benzilmonoximethiocarbohydrazide (HBMT) Schiff bases as multifunctional scaffolds with concurrent antimalarial, antioxidant, and selective cytotoxic activities. The lead derivative, **HBMT-3M4HB**, demonstrated sub-micromolar potency against *Plasmodium falciparum* 3D7 (IC_{50} = 1.24 μM), strong antioxidant capacity (DPPH IC_{50} = 6.42 μM; FRAP = 948.2 μmol Fe^{2+} per mg), and selective cytotoxicity against MCF-7 cells (IC_{50} = 21.6 μM) with reduced toxicity toward normal HEK-293 cells (IC_{50} = 58.3 μM). This rare triad of pharmacological properties within a single chemical scaffold underscores its translational relevance for complex pathologies where infection, oxidative stress, and abnormal cell survival are interconnected.

From a drug discovery perspective, these findings position HBMT Schiff bases as lead-like chemical matter. Computational ADMET profiling predicted good oral bioavailability, acceptable solubility, and low toxicity, while docking and molecular dynamics studies indicated strong and stable binding to biologically relevant targets. These complementary datasets provide confidence in the scaffold's suitability for further development.

Future research will focus on *in vivo* antimalarial efficacy, detailed pharmacokinetic studies, and structural optimization guided by SAR to improve selectivity and potency. The dual antioxidant and pro-apoptotic mechanisms also suggest applications beyond malaria, particularly in cancers characterized by oxidative imbalance. Expanding this scaffold into hybrid or conjugated systems may further enhance activity while modulating drug-like properties.

Taken together, the present study provides a robust foundation for advancing HBMT Schiff bases toward preclinical development and exemplifies the value of integrating synthetic chemistry, mechanistic biology, and computational modeling in the discovery of multifunctional therapeutic agents.

4. Conclusions

This study provides the first integrated evaluation of benzilmonoximethiocarbohydrazide (HBMT) Schiff bases as multifunctional therapeutic scaffolds. The four synthesized derivatives were obtained in high yields (75–80%) and validated for structural integrity and chromatographic purity (>98.8%). Biological evaluation revealed potent antimalarial activity, with **HBMT-3M4HB** emerging as the most active candidate (IC_{50} = 1.24 ± 0.08 μM), approaching chloroquine (0.28 ± 0.03 μM), while other derivatives displayed IC_{50} values of 1.97–3.07 μM. In antioxidant assays, **HBMT-3M4HB** exhibited superior efficacy (DPPH IC_{50} = 6.42 ± 0.11 μM; FRAP = 948.2 ± 12.7 μmol Fe^{2+} per mg), while cytotoxicity testing demonstrated selective activity toward MCF-7 cells (IC_{50} = 21.6–32.8 μM) over HEK-293 cells (58.3–71.7 μM).

Mechanistic studies confirmed apoptosis induction through Bax and caspase-3 activation with concomitant suppression of Bcl-2, NF-κB p65, and iNOS, coupled with HO-1 upregulation. Computational analyses supported these findings: DFT revealed favorable electronic descriptors, docking predicted strong interactions (ΔG_{bind} up to −72.1 kcal mol^{-1}), and 500 ns molecular dynamics simulations established complex stability. ADMET predictions indicated favorable bioavailability and low toxicity.

Together, these results establish HBMT Schiff bases as a promising chemical class with a rare combination of antimalarial potency, antioxidant efficacy, and selective cytotoxicity. The strong correlation between experimental and computational findings underscores their translational potential, positioning **HBMT-3M4HB** as a compelling lead for future *in vivo* and preclinical development.

Author contributions

Shravan Kumar Singh: synthesis, characterization, writing original draft (synthesis, characterization), data curation, investigation, conceptualization, methodology, validation, and funding. Abhay Bagul: writing – review and editing, data curation, investigation, visualization and validation. Manish Kumar: writing review and editing. Aisha Tufail: writing the original draft (*in silico* work), visualization, validation. Santosh Waman Kulkarni: validation, and formal analysis. Sheetal Sharma: supervision (synthesis, characterization, biological activities) validation, conceptualization and formal analysis. Amit Dubey: supervision (computational work and biological), conceptualization, writing the original draft (*in silico* work and biological activities), software (molecular docking, DFT, MESP, pharmacophore modeling and ADMET), visualization, methodology, writing – review and editing, validation and formal analysis.

Conflicts of interest

The authors declare no competing financial interest.

Data availability

The data supporting this article have been included as part of the supplementary information (SI). Supplementary information is available. See DOI: **https://doi.org/10.1039/d5ra06425b**.

Acknowledgements

This research did not receive any specific grant from funding agencies in the public, commercial, or not-for-profit sectors.

References

1 M. S. Çavuş, H. Yakan, C. Başkan, H. Muğlu and A. A. Babacan, *J. Mol. Struct.*, 2024, **1304**, 137655.
2 S. M. Shahcheragh, A. Habibi, M. Shirzad, Y. Farahani and S. Sardari, *Health Biotechnol. Biopharma.*, 2023, **6**, 81–97.
3 N. Georgiou, E. Chontzopoulou, A. Cheilari, A. Katsogiannou, D. Karta, K. Vavougyiou, D. Hadjipavlou-Litina, U. Javornik, J. Plavec, D. Tzeli, S. Vassiliou and T. Mavromoustakos, *ACS Omega*, 2023, **8**, 11966–11977.
4 G. S. Mrđan, S. S. Vlaisavljević, P. N. Knežević, I. N. Nikolić, D. G. Tenji and B. M. Matijević, *J. Serb. Chem. Soc.*, 2025, **90**, 1–12.
5 M. A. Abd Ul-Malik, A. Abdou, M. R. Fouad, A. S. N. Alkamali and S. A. A. Abdel-Raheem, *Curr. Chem. Lett.*, 2024, **13**, 683–694.
6 W. Tabor, A. Katsogiannou, D. Karta, E. Andrianopoulou, Ł. Berlicki, S. Vassiliou and A. Grabowiecka, *ACS Omega*, 2023, **8**, 28783–28796.
7 K. K. Mohammed Hashim, E. Manoj and M. R. Prathapachandra Kurup, *ChemistrySelect*, 2022, **7**, 1229.
8 I. N. Cvijetić, B. Herlah, A. Marinković, A. Perdih and S. K. Bjelogrlić, *Pharmaceuticals*, 2023, **16**, 341.
9 Y. Kaya, O. Sacan, A. Erçağ and R. Yanardag, *Indian J. Chem.*, 2022, **61**, 895–900.
10 N. Georgiou, A. Katsogiannou, D. Skourtis, H. Iatrou, D. Tzeli, S. Vassiliou, U. Javornik, J. Plavec and T. Mavromoustakos, *Molecules*, 2022, **27**, 2537.
11 S. Aldulaijan, S. Nabil, S. Alharthi, B. A. L. Abdullatif and A. S. Abdel-Naby, *New J. Chem.*, 2023, **47**, 13367–13377.
12 M. H. Assaleh, S. K. Bjelogrlić, N. Prlainovic, I. Cvijetić, A. Bozic, I. Arandjelovic, D. Vukovic and A. Marinkovic, *Arab. J. Chem.*, 2022, **15**, 103532.
13 S. Kumar, P. Sekar and S. K. Raju, *Adv. Pharm. J.*, 2023, **8**, 1–16.
14 L. V. Menon and E. Manoj, *J. Mol. Struct.*, 2025, **1330**, 141497.
15 L. V. Menon and E. Manoj, *J. Fluoresc.*, 2025, **35**, 4363–4375.
16 E. A. E. El-Helw, *et al.*, *Polycycl. Aromat. Compd.*, 2025, **45**, 1431–1446.
17 B. S. Baaiu, N. M. Saleh, A. F. AlshrefAldirsi and A. Abdel-Aziem, *Future Med. Chem.*, 2025, **17**, 9–18.

18 N. Zaware, N. Rasal, V. Lambate and S. Jagtap, *Bioorg. Med. Chem. Lett.*, 2025, **118**, 130079.
19 S. Tripathi, M. Kumar, A. Tufail, P. Chauhan and A. Dubey, *Nanoscale*, 2025, **17**, 19455–19474.
20 A. Ram, A. Pandey, G. Singh, M. Kumar, P. Bharati, M. Jaiswal, P. Niranjan, Y. Kumar, P. Rawat and R. N. Singh, *Spectrosc. Lett.*, 2025, **58**, 1–23.
21 M. Leidenberger, C. Voigtländer, N. Simon, and B. Kappes, *Cell Viability Assays: Methods and Protocols*, Springer, New York, 2017, pp. 97–110.
22 J. D. Johnson, R. A. Dennull, L. Gerena, M. Lopez-Sanchez, N. E. Roncal and N. C. Waters, *Antimicrob. Agents Chemother.*, 2007, **51**, 1926–1933.
23 S. Karl, R. P. Wong, T. G. St Pierre and T. M. Davis, *Malar. J.*, 2009, **8**, 294.
24 A. Dubey, M. Kumar, A. Tufail and A. D. Bagul, *RSC Adv.*, 2025, **15**, 18777–18801.
25 M. Kumar, V. Pratap, M. K. Singh, A. K. Nigam, P. Kumar and J. I. Kumar, *J. Life Sci. Res.*, 2015, **7**, 2901–2907.
26 I. F. Benzie and M. Devaki, *Meas. Antioxid. Act. Capacity*, 2018, 77–106.
27 D. Msalbi, F. Jellali, J. Elloumi-Mseddi, B. Hakim, E. Sahli and S. Aifa, *Med. Oncol.*, 2023, **40**, 309.
28 M. Kumar, K. Pal, V. Pratap and J. K. Gour, *J. Sci. Res.*, 2022, **66**, 129–141.
29 M. Izdebska, W. Zielińska, A. Krajewski, M. Hałas-Wiśniewska, K. Mikołajczyk, M. Gagat and A. Grzanka, *Int. J. Mol. Sci.*, 2021, **22**, 12783.
30 L. Zhao, H. Luo, X. Li, T. Li, J. He, Q. Qi and Z. Yu, *Cardiology*, 2017, **137**, 43–53.
31 K. Sopitthummakhun, C. Thongpanchang, T. Vilaivan, Y. Yuthavong, P. Chaiyen and U. Leartsakulpanich, *Malar. J.*, 2012, **11**, 194.
32 T. Thavayogarajah, P. Gangopadhyay, S. Rahlfs, K. Becker, K. Lingelbach, J. M. Przyborski and A. A. Holder, *PLoS One*, 2015, **10**, e0125191.
33 F. A. Al-Temimei, M. T. Awayiz and H. I. Abbood, *J. Fluoresc.*, 2024, **34**, 1–13.
34 S. K. Singh, A. Bagul, A. Tufail, M. S. Ali, A. Ragusa, S. W. Kulkarni and A. Dubey, *Appl. Organomet. Chem.*, 2025, **39**, e70286.
35 V. Choudhary, A. Bhatt, D. Dash and N. Sharma, *J. Comput. Chem.*, 2019, **40**, 2354–2363.
36 A. K. Maddheshiya, M. Kumar, A. Tufail, P. S. Yadav, Y. Deswal, N. Yadav and A. Dubey, *ACS Appl. Bio Mater.*, 2024, **7**, 5906–5924.
37 S. R. Gadre, C. H. Suresh and N. Mohan, *Molecules*, 2021, **26**, 3289.
38 A. Bagul, M. Kumar, A. Tufail, N. Tufail, D. Gaikwad and A. Dubey, *Appl. Organomet. Chem.*, 2024, **38**, e7521.
39 N. Drinkwater, R. S. Bamert, K. K. Sivaraman, A. Paiardini and S. McGowan, *Proteins:Struct., Funct., Bioinf.*, 2015, **83**, 789–795.
40 W. Yang, B. T. Riley, X. Lei, B. T. Porebski, I. Kass, A. M. Buckle and S. McGowan, *ChemMedChem*, 2018, **13**, 2504–2513.
41 K. Lestari, T. Sitorus, S. M. Instiaty and J. Levita, *J. Adv. Pharm. Educ. Res.*, 2020, **10**, 2.
42 A. D. Bagul, M. Kumar, A. M. Alanazi, A. Tufail, N. Tufail, D. D. Gaikwad and A. Dubey, *BioMetals*, 2024, **37**, 1713–1737.
43 A. Dubey, V. Singh, P. K. Doharey, M. P. Sk, S. K. Samanta, V. Nema and A. K. Sahoo, *Int. J. Biol. Macromol.*, 2021, **170**, 523–531.
44 B. Kumar, J. Devi, A. Dubey and M. Kumar, *Chem. Biodivers.*, 2024, **21**, e202401116.
45 N. Bhusari, A. Bagul, V. K. Mishra, A. Tufail, D. Gaikwad and A. Dubey, *RSC Adv.*, 2025, **15**, 22764–22788.
46 Z. Deng, C. Chuaqui and J. Singh, *J. Med. Chem.*, 2004, **47**, 337–344.
47 P. K. Doharey, P. Verma, A. Dubey, S. K. Singh, M. Kumar, T. Tripathi and B. Sharma, *J. Biomol. Struct. Dyn.*, 2024, **42**, 1533–1543.
48 S. Stevanović, A. Perdih, M. Senćanski, S. Glišić, M. Duarte, A. M. Tomas and T. Solmajer, *Molecules*, 2018, **23**, 772.
49 S. Tripathi, M. Kumar, A. Tufail, P. Chauhan and A. Dubey, *Chem. Eng. J.*, 2025, **521**, 167034.
50 A. Dubey, M. Kumar, A. Tufail, V. D. Dwivedi and A. Ragusa, *J. Infect. Public Health*, 2025, **18**, 102885.
51 D. Petrović, X. Wang and B. Strodel, *Proteins:Struct., Funct., Bioinf.*, 2018, **86**, 935–944.
52 C. Zhang, S. Raugei, B. Eisenberg and P. Carloni, *J. Chem. Theory Comput.*, 2010, **6**, 2167–2175.
53 A. Dubey, A. M. Alanazi, R. Bhardwaj and A. Ragusa, *Mol. Divers.*, 2024, **28**, 1–16.
54 H. H. Refsgaard, B. F. Jensen, P. B. Brockhoff, S. B. Padkjær, M. Guldbrandt and M. S. Christensen, *J. Med. Chem.*, 2005, **48**, 805–811.
55 H. Sardar, *Phytonutrients*, 2023, **2**, 2–8.
56 A. P. Byrnes, S. Zhang, L. Canter, M. D. Sonnenfeld, in *Unconv. Resour. Technol. Conf.*, Austin, Texas, 2017, pp. 1584–1603.
57 S. K. Singh, A. Bagul, A. Tufail, P. Alam, S. W. Kulkarni, S. Sharma and A. Dubey, *BioMetals*, 2025, **38**, 245–274.
58 G. R. Burns, *Inorg. Chem.*, 1968, **7**, 277–283.
59 S. K. Singh, A. Bagul, A. Tufail, M. S. Ali, A. Ragusa, S. W. Kulkarni, S. Sharma and A. Dubey, *Appl. Organomet. Chem.*, 2025, **39**, e70286.
60 M. Yaswant, A. Dubey, A. Tufail, S. Nath, S. Janardhan, M. Maffia, A. Ragusa and V. K. Mishra, *Sci. Rep.*, 2025, **15**(33906).
61 A. Dubey, M. Kumar, A. Tufail, V. D. Dwivedi and A. Ragusa, *Bioinorganic Chemistry and Applications*, 2025, (6680612), 22.
62 R. M. Silverstein, F. X. Webster, and D. J. Kiemle, *Spectrometric Identification of Organic Compounds*, Wiley, New York, 7th edn, 2005.